

Experimental investigation on vortex-induced force of a Steel Catenary Riser under in-plane vessel motion

Mengmeng Zhang ^{a,b}, Shixiao Fu ^{a,b,*}, Chang Liu ^c, Haojie Ren ^{a,b}, Yuwang Xu ^{a,b}

^a State Key Laboratory of Ocean Engineering, Shanghai Jiao Tong University, Shanghai, 200240, China

^b Collaborative Innovation Centre for Advanced Ship and Deep-Sea Exploration, Shanghai, 200240, China

^c Department of Mechanical Engineering, Johns Hopkins University, Baltimore, MD, 21218, USA

ARTICLE INFO

Keywords:

Vessel motion-induced vibration
Steel catenary riser
Vortex-induced forces
Time-varying excitation coefficients
Time varying added mass coefficients

ABSTRACT

A method to identify vortex-induced forces and coefficients from measured strains of a Steel Catenary Riser (SCR) undergoing vessel motion-induced Vortex-induced Vibration (VIV) is proposed. Euler–Bernoulli beam vibration equations with time-varying tension is adopted to describe the out-of-plane VIV responses. Vortex-induced forces are reconstructed via inverse analysis method, and the Forgetting Factor Least Squares (FF-LS) method is employed to identify time-varying vortex-induced force coefficients, including excitation coefficients and added mass coefficients. The method is verified via a finite element analysis procedure in commercial software Orcaflex. The time-varying excitation coefficients and added mass coefficients of an SCR undergoing vessel motion-induced VIV are investigated. Results show that vessel motion-induced VIV is excited at the middle or lower part of the SCR and in the acceleration period of in-plane velocity, where most of the excitation coefficients are positive, while during the deceleration period, the excitation coefficients becomes too small to excite VIVs. Parameter γ [1] has strong correlation with excitation coefficients. In addition, time-varying tensions contribute significantly to the variations of added mass coefficients under the condition that the ratio of dynamic top tension to pretension exceeds the range of 0.7–1.3. Moreover, chaotic behaviors are observed in vortex-induced force coefficients and are more evident with the increase of vessel motion velocity. This behavior may attribute to the randomness existing in in-plane velocity and its coupling with out-of-plane vibrations.

1. Introduction

As oil and natural gas exploration and production extend to increasingly deep waters, the cost of the riser systems and technological challenges increase rapidly. The use of compliant risers such as the Steel Catenary Riser (SCR) and the Steel Lazy Wave Riser (SLWR) are efficient solutions for deep-water oil and gas production systems. An SCR is a prolongation of a sub-sea pipeline attached to a floating production structure in a catenary configuration. The first SCR was installed by Shell in the Auger tension leg platform (TLP) in 1994 at a water depth of 872 m [2].

It is well known that under the action of ocean currents, vortices are generated and alternately shed from the sides of the SCR [3]. This vortex shedding leads to periodic pressure variation around the risers, producing a Vortex-induced Force (VIF). If the frequency of

* Corresponding author. State Key Laboratory of Ocean Engineering, Shanghai Jiao Tong University, Shanghai, 200240, China.
E-mail address: shixiao.fu@sjtu.edu.cn (S. Fu).

the vortex-induced force is near one of the natural frequencies of the risers, a significant vibration will be induced in the risers, which is normally termed as Vortex-induced Vibration (VIV). In addition to this ocean current induced VIV, purely in-plane vessel motion at the top of the SCR was found to introduce out-of-plane VIVs, termed as vessel motion-induced VIVs [4–7], which occur because the riser will be exposed to the oscillatory flow field due to its motions in still water, even without the existence of ocean currents. Once the shedding frequency under relatively oscillatory flow approximates the riser natural frequency, the riser will further experience intermittent out-of-plane vibration. Such vessel motion-induced VIVs were recognized to greatly amplify the riser fatigue damages compared with the global dynamic response under vessel motion, and would lead to more fatigue damage than steady ocean flow induced VIVs [6]. These new findings indicated the necessities of including vessel motion induced VIVs during the riser design.

So far, there has been some researches on VIV in oscillatory flow in order to understand vessel motion-induced VIV. Sumer and Fredsøe (1988) carried out VIV tests of an elastically mounted rigid cylinder exposed to an oscillating flow with the Keulegan-Carpenter (KC) number range $5 \leq KC \leq 100$ and the reduced velocity V_r ranging from 0 to 16. Various vibrational response patterns were observed for cases with different KC numbers. The response characteristics of the cylinder have been shown to vary extensively, depending on KC number as well as on the reduced velocity. Lodahl et al. (1998) fixed the oscillating mechanism in the U-shaped water tank and generated an oscillating flow field through the U-shaped water tank to drive the cylinder to vibrate in the cross flow direction. The results showed that the vortex-induced vibration response of a cylinder under oscillating flow depended on both the KC number and the maximum reduced velocity $V_{r\max}$. The number of vortex shedding pairs in each oscillating flow cycle, which was the ratio of vortex-induced vibration response frequency and oscillation frequency, was closely related to the KC number and $V_{r\max}$. Fernandes et al. [8] simulated a relative oscillating flow field by forcing an entire oscillating device to oscillate in still water. It was found that as the KC number increased (from 10 to 40), the cylinder motion trajectory transitioned from "I" to "ellipse", "8", "three rings", "four rings" and "S". However, the experimental results of Lodahl et al. [9] and Fernandes et al. [8] were still based on the premise that the vortex-induced vibration response frequency was constant. The time histories of VIV frequencies were not analyzed in detail to study the possible "time-sharing characteristics". Fu et al. [10] conducted a model test of a flexible cylinder in oscillatory flow to ascertain the VIV response characteristics under different KC numbers and maximum reduced velocities. More novel phenomena of VIV under oscillatory flows were found: unsteady VIV with three developing stages steps of "building up - locking in - dying out", modulated VIV amplitudes, hysteresis of motion trajectories, and time-sharing frequencies. Ren et al. [11] further conducted a series of VIV model tests for a straked flexible pipe under oscillatory flow with different KC numbers and reduced velocities V_r . The suppression efficiency of strakes under oscillatory flow when the KC number was smaller than 40 and reduced velocity was larger than 6, was found to be not as good as that under uniform flow. More investigations were suggested to evaluate suppression efficiencies of strakes with different pitches and heights under oscillatory flow. In addition, there was research focusing on prediction methods for VIV under oscillatory flow. Chang et al. (2003) predicted the VIV of flexible pipes under heave motion of the platform based on the wake oscillator and discrete vortex model. Liao [12] adopted the reduced damping parameter S_g and the wave propagation parameter $n\zeta$ to predict such VIV. However, the accuracy of these two predictions have not been examined by the model test [13,14]. proposed a resonant mechanism between the phase transition of vortex-induced forces and velocities to realize the real-time prediction of the vortex-induced force and then solved the structure governing equations to predict VIV responses of the SCR under in-plane motions. The adopted vortex-induced force coefficients model, however, was obtained from VIV tests under uniform flow, which may not be valid for an SCR under vessel motion induced VIV, further causing a lack of accuracy and feasibility for this method. Although academics have launched certain numerical and experimental research on response features and prediction methods on VIVs under oscillatory flow, the force mechanism that plays an important role in the understanding and prediction of VIVs remains undiscovered and key input parameters for vessel motion induced VIV force coefficients model are still unclear.

At present, researches on the vortex-induced forces of risers have been focused on those under steady flows. Gopalkrishnan [15] and Aronsen [16] experimentally investigated the hydrodynamic forces on a cylinder under forced oscillation at pure Cross-flow (CF) and pure In-line (IL) directions, respectively. Dahl [17] conducted two-dimensional forced oscillation tests of rigid cylinder to systematically investigate the hydrodynamics of flexible risers under coupled VIV responses in CF and IL directions. Yin et al. [18] performed forced oscillation tests on a full-scale rigid riser under prototype Re number ($\sim 6 \times 10^5$) in a purely CF direction. Distribution of excitation coefficients along non-dimensional frequency and amplitude ratios under prototype Re number ($\sim 4 \times 10^5$) is different from that under low Re numbers. This finding strongly indicated that Re number effects should be considered in offshore riser/pipeline design. The above hydrodynamic coefficients were all obtained from rigid cylinder tests, which missed the spanwise correlation of vortex shedding what the real flow field has. To reveal such discrepancies, Wu et al. (2007) obtained the vortex-induced forces and its coefficients on a flexible riser in the CF direction using an inverse method. Combining the modal analysis method and the Euler-Bernoulli beam vibration equations, Song et al. [19] analyzed the hydrodynamic force of a flexible riser using the strain information measured in the scaled model test. The results indicated great differences between the real coefficients on a flexible pipe vibrating in 3D and conventional ones obtained through 2D forced oscillation tests. Zhang et al. [20] and Fu et al. [21] further discovered great ramps of VIV hydrodynamic coefficients between the bare cylinder and the adjacent buoyancy elements, where the added mass coefficient could reach up to 40, which has been proved to be within the same level as those observed by forced oscillation tests by Wu et al. [22]. Liu et al. [23] further proposed the Forgetting Factor Least Squares (FF-LS) method to identify time-varying VIF coefficients of a flexible riser under multi-frequency and time-sharing frequency vortex-induced vibrations (VIV). The coupling effect between the basic frequency and high frequency were qualified. However, the above methods have three limitations: 1) The optimization analysis to identify hydrodynamic coefficients in Wu's (2007), Song's (2016) and others' methods [20,21] is carried out for the entire time period, which cannot process the case with time-varying features of VIV amplitudes, frequencies and hydrodynamic coefficients. Generally, the displacement signals in above method need to be bandpass filtered around the Strouhal frequency to achieve acceptable optimization results. But for signals with time-sharing frequency characteristics, this process would easily change

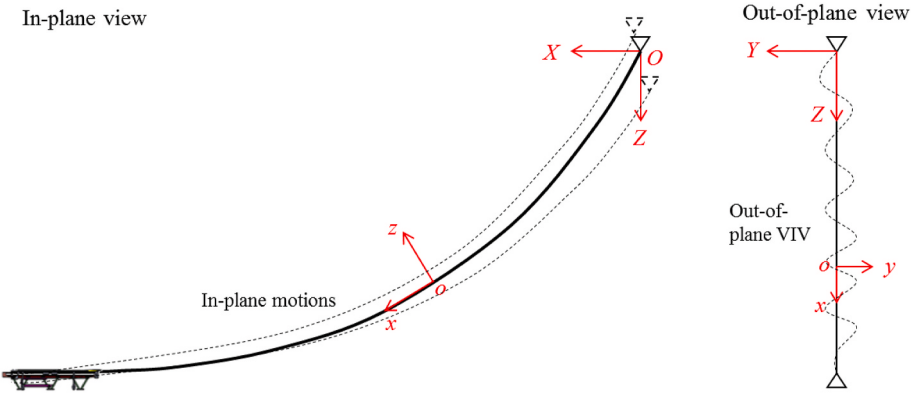


Fig. 1. Coordinate systems of a SCR under in-plane vessel motions.

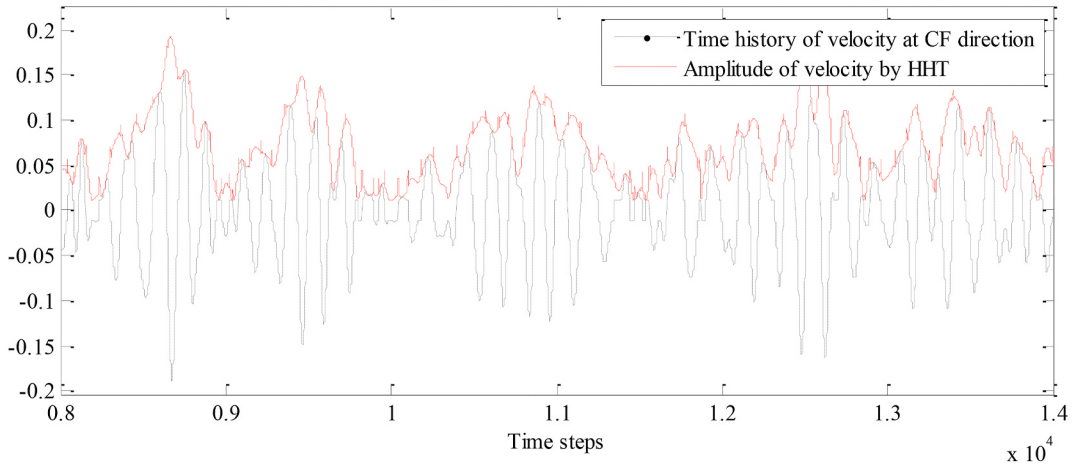


Fig. 2. Time history of CF velocity at one node and the corresponding amplitude by HHT.

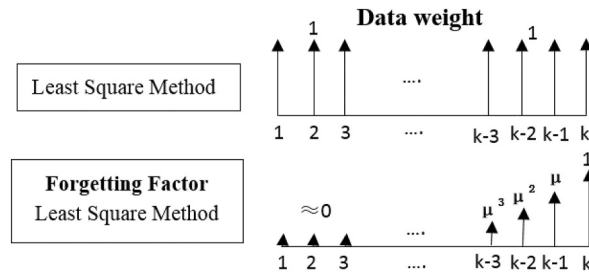


Fig. 3. Schematic of data weight for forgetting factor least square method.

the signal phases, resulting in signal distortion. 2) The spatial-temporal variation characteristics of tension were not considered. For methods which used FE equations with mass matrix M, damping matrix C and stiffness matrix K to express the VIV responses of a riser, it is time consuming and highly computational cost to update stiffness matrix K and damping matrix C at each time step to take the spatial-temporal tension variations into consideration. 3) The mass, damping and stiffness matrixes (M, C, K) need to be established in a unified global coordinate system, and the spatial coordinates for each node and the coordinate transform matrix of each element relative to the global coordinate system should be known. However, the spatial configuration of a SCR and its variations under vessel motions in model tests cannot be directly measured or accurately reconstructed, which means that the use of the MCK matrix in above mentioned inverse methods is not feasible for vortex-induced forces identification of a SCR undergoing vessel motion-induced VIV. The above three limitations make the present inverse methods infeasible for vessel motion induced VIV force identification of an SCR.

This paper proposed a vortex-induced forces and coefficients identification method for an SCR undergoing vessel motion-induced

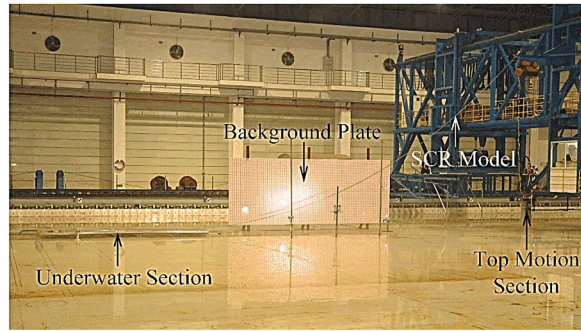


Fig. 4. Overview of the experimental setup.

Table 1
Physical properties of the considered SCR.

Item	Measured Value of Test Model
Total Length (m)	23.71
Water Depth (m)	9
Length of Sag-bend (m)	21.0806
Horizontal Length of Flow Line (m)	2.626
Horizontal Length of Sag-bend (m)	18.4175
Outer Diameter (m)	0.024
Mass per unit length in Air (kg/m)	0.69
Mass Ratio	1.53
Bending Stiffness EI (Nm ²)	10.5
Tensile Stiffness EA (N)	6.67×10^5
Damping ratio	1.4%

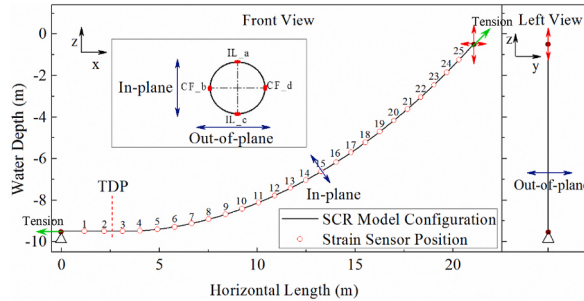
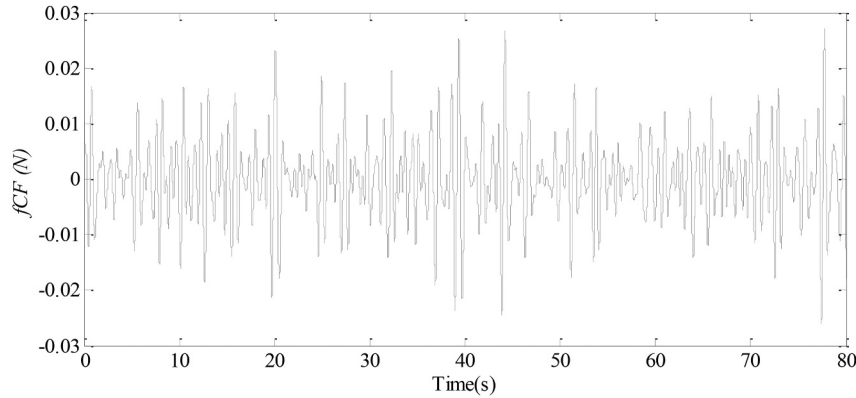


Fig. 5. Truncated SCR model configuration and strain sensor locations.

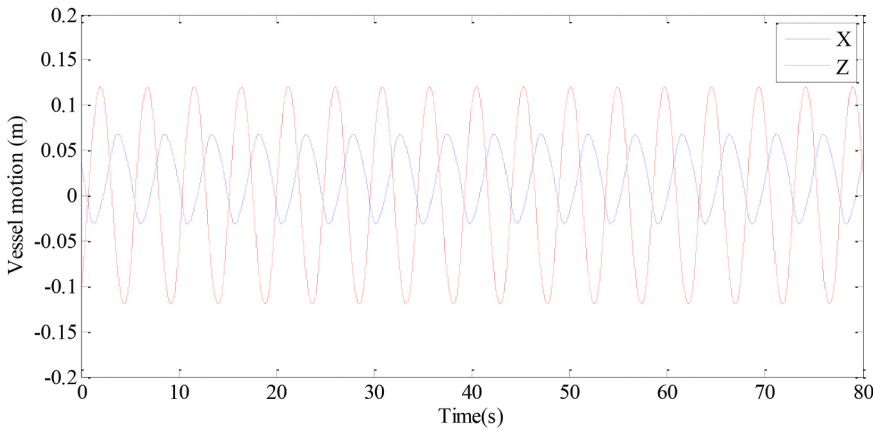
Table 2
Test matrix.

Case Name	Heave motion amplitude A_{im} (m)	Period Tim (s)
H A0105T481	0.105	4.81
H A0105T596	0.105	5.96
H A021T596	0.21	5.96

VIV. In this method, Euler–Bernoulli beam vibration equations with spatial-temporally varying tension was adopted to describe the out-of-plane VIV responses. Vortex-induced responses and forces were reconstructed via inverse analysis method based on measured strain signals in SCR model tests (Section 2.1). Then, the Forgetting Factor Least Squares (FF-LS) method was employed to identify time-varying vortex-induced force coefficients, including excitation coefficients and added mass coefficients. The method was verified via a finite element analysis procedure in well-validated commercial software Orcaflex (Section 4). Features of the time-varying excitation coefficients and added mass coefficients of a SCR undergoing vessel motion-induced VIV were discussed in Section 5.



(a) Time history of the applied force at 7.5m of SCR numerical model in Orcaflex



(b) Time history of the forced vessel motion at top of SCR numerical model in Orcaflex

Fig. 6. Time history of applied force at one node and forced vessel motion at top of SCR numerical model (Case H A0105T481).

2. Vortex-induced force identification method

2.1. Inverse analysis method for hydrodynamic force

The in-plane and out-of-plane view of a steel catenary riser is illustrated in Fig. 1. The X-Z plane of global Cartesian coordinate system O-XYZ is set to be in in-plane, and the Y-Z plane is in the out-of-plane. Meanwhile, a local coordinate system o-xyz whose x axis lies on the central axis of SCR and x-z plane is parallel to X-Z plane of the global Cartesian coordinate system is defined. The y axis is orthogonal to x-z plane and is defined as the CF direction.

Under in-plane vessel motions, the SCR will experience relatively oscillatory flow due to its motions in in-plane direction (X-Z plane). The oscillatory flow has been proved to induce VIV responses in the out-of-plane direction [24]. Such kinds of VIV still belong to the small displacement and small deformation problems; thus, it can be described by Euler-Bernoulli beam, an equation with time-varying tension in local coordinate system:

$$EI \frac{\partial^4 y(x, t)}{\partial x^4} - \frac{\partial}{\partial x} \left[T(x, t) \frac{\partial y(x, t)}{\partial x} \right] + c \frac{\partial y(x, t)}{\partial t} + m \frac{\partial^2 y(x, t)}{\partial t^2} = f_{CF}(x, t), \quad (1)$$

where EI is the bending stiffness; m is the mass per unit length; c is the structural damping factor; $c = 2m\omega\zeta$ ζ is the structural damping ratio; ω is the dominant oscillation frequency of SCR, which is obtained from measured strains using Fast Fourier Transform (FFT). $T(x, t)$ is the spatial-temporal tension at section x of time step t, which is calculated by superposition of measured tensile strain multiplying tensile stiffness and the measured pretension at each measuring stations. $f_{CF}(x, t)$ is the periodic vortex-induced force. $y(x, t)$ is the displacement of SCR in the CF direction due to VIV, which can be obtained from measured strain responses via modal superposition method [19]. In this paper, the static SCR configuration and static tension distribution is considered in modal shape calculation. Then, all of the temporal and spatial differentiation in Eq. (1) can be obtained by finite difference method.

The feasibility of the proposed inverse method for hydrodynamic force above was validated by applying identified forces and

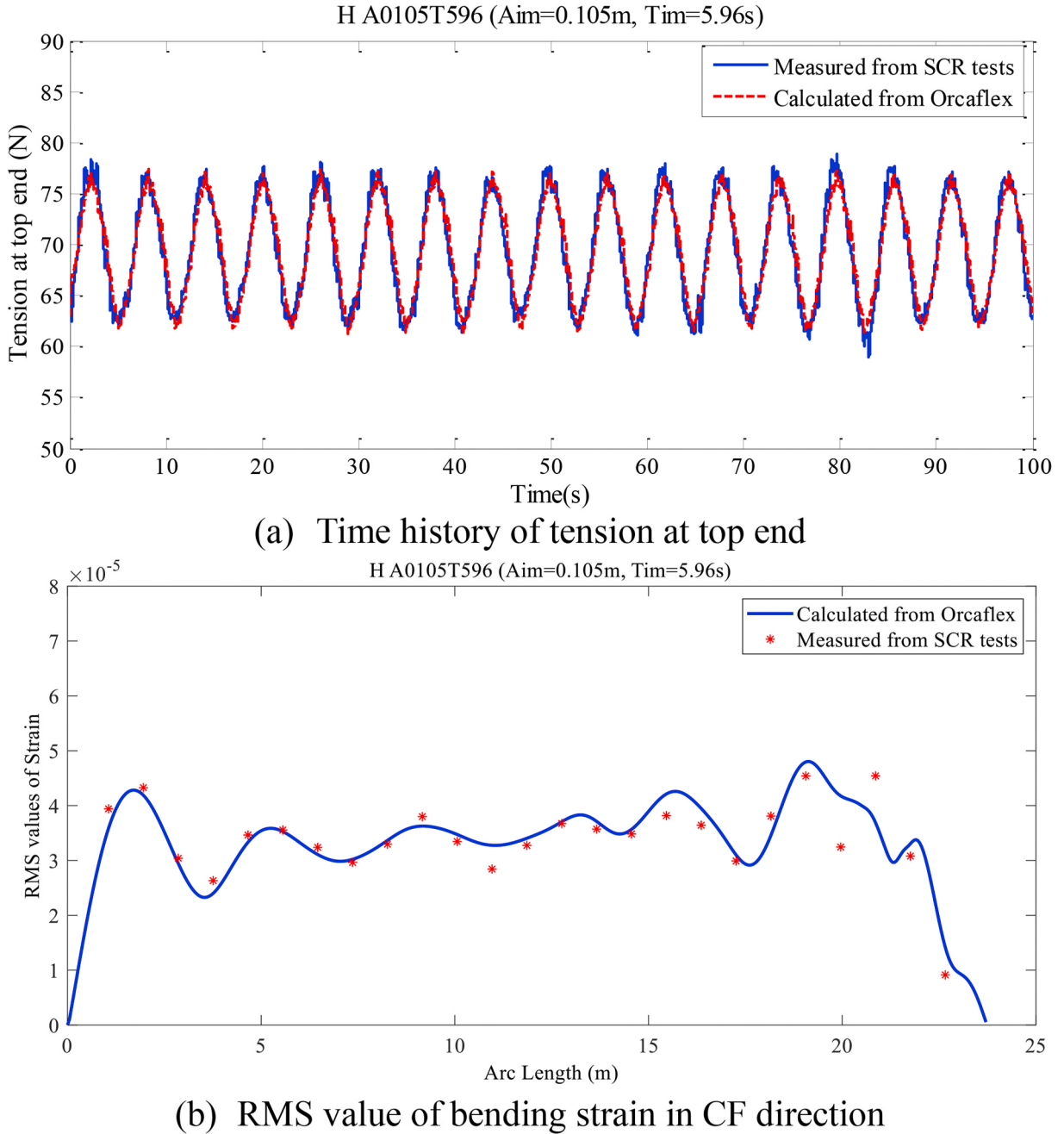


Fig. 7. Axial distributions of the measured and calculated dynamic responses (Case H A0105T596).

predefined in-plane vessel motions on the SCR finite element model in Orcaflex [25]. A detailed description can be found in Section 4.

2.2. Vortex-induced force coefficient identification

The definition of vortex-induced force proposed by Sarıkaya [26] and widely used in current prediction tools [27,28] has two terms, which are excitation force in phase with velocity and added mass force in phase with acceleration, as shown in Eq. (2),

$$f_{CF}(x, t) = \frac{1}{2} \rho D U^2(x) C_e(x) \frac{\dot{y}(x, t)}{|\dot{y}(x, t)|} - \frac{\pi D^2}{4} \rho C_a(x) \ddot{y}(x, t), \quad (2)$$

where ρ is fluid density; D is the diameter of cylinder or pipe; $U(x)$ is the flow speed at location x on the pipe; $\dot{y}(x, t)$ and $\ddot{y}(x, t)$ are

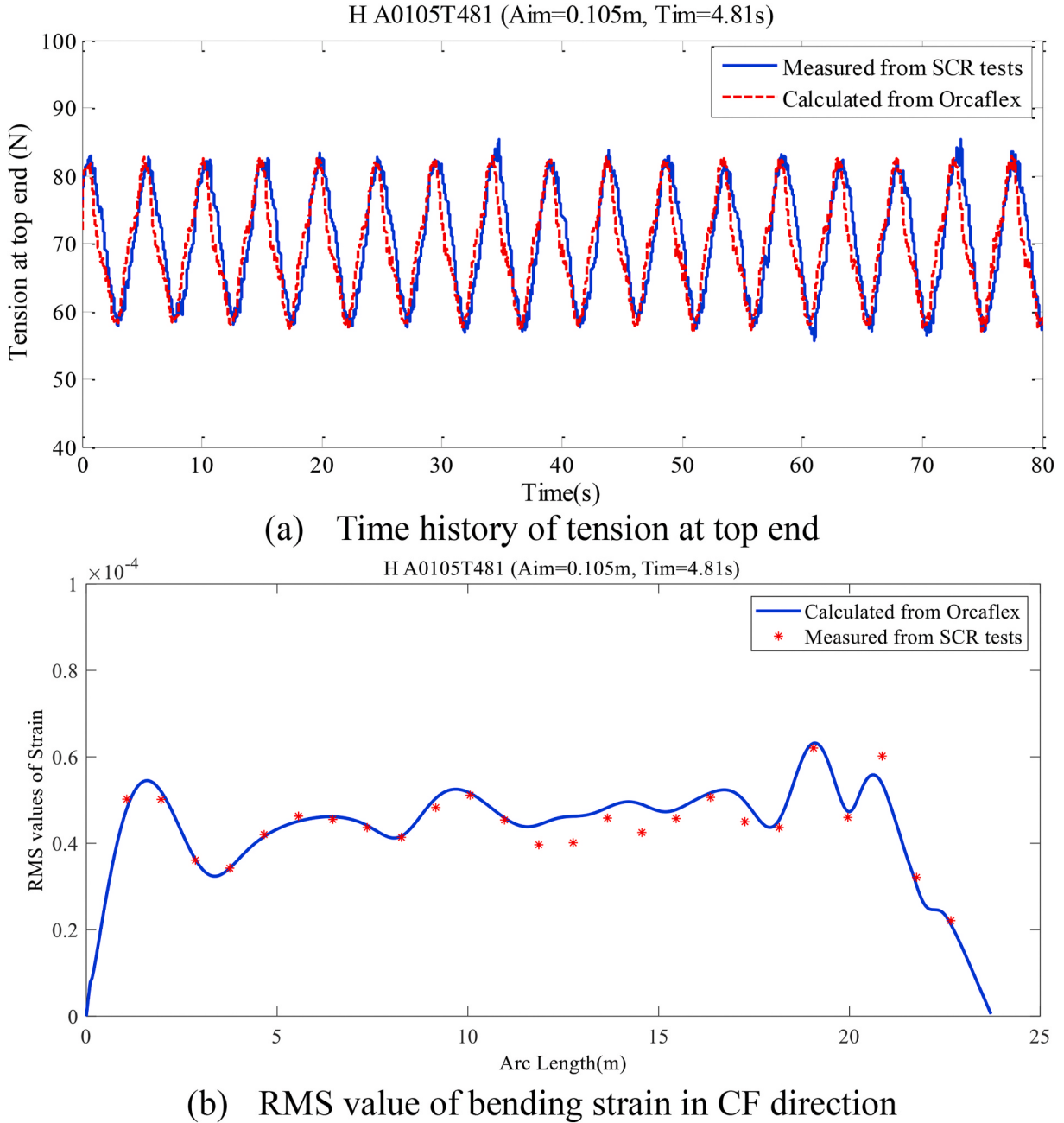


Fig. 8. Axial distributions of the measured and calculated dynamic responses (Case H A0105T481).

velocity and acceleration at location x , respectively. $|\dot{y}(x, t)|$ means amplitude of velocity. $Ce(x)$ is the excitation coefficient, and $Ca(x)$ is added mass coefficients, both of which do not change with time.

When an SCR undergoes in-plane vessel motion, out-of plane VIV will be excited [24]. Multi-frequency coupling, amplitude modulation, and time-sharing frequency [6,10,29] are usually observed in vessel motion-induced VIV. Time-invariant hydrodynamic coefficients, which average varying information in the time domain, cannot consider these time-sharing effects of vessel motion-induced VIV.

In this study, we change time-invariant hydrodynamic coefficients into time-varying coefficients as we attempt to capture the time-sharing amplitude and frequency effects in vortex-induced vibration under oscillatory flow. The time-varying hydrodynamic coefficient problem is defined as:

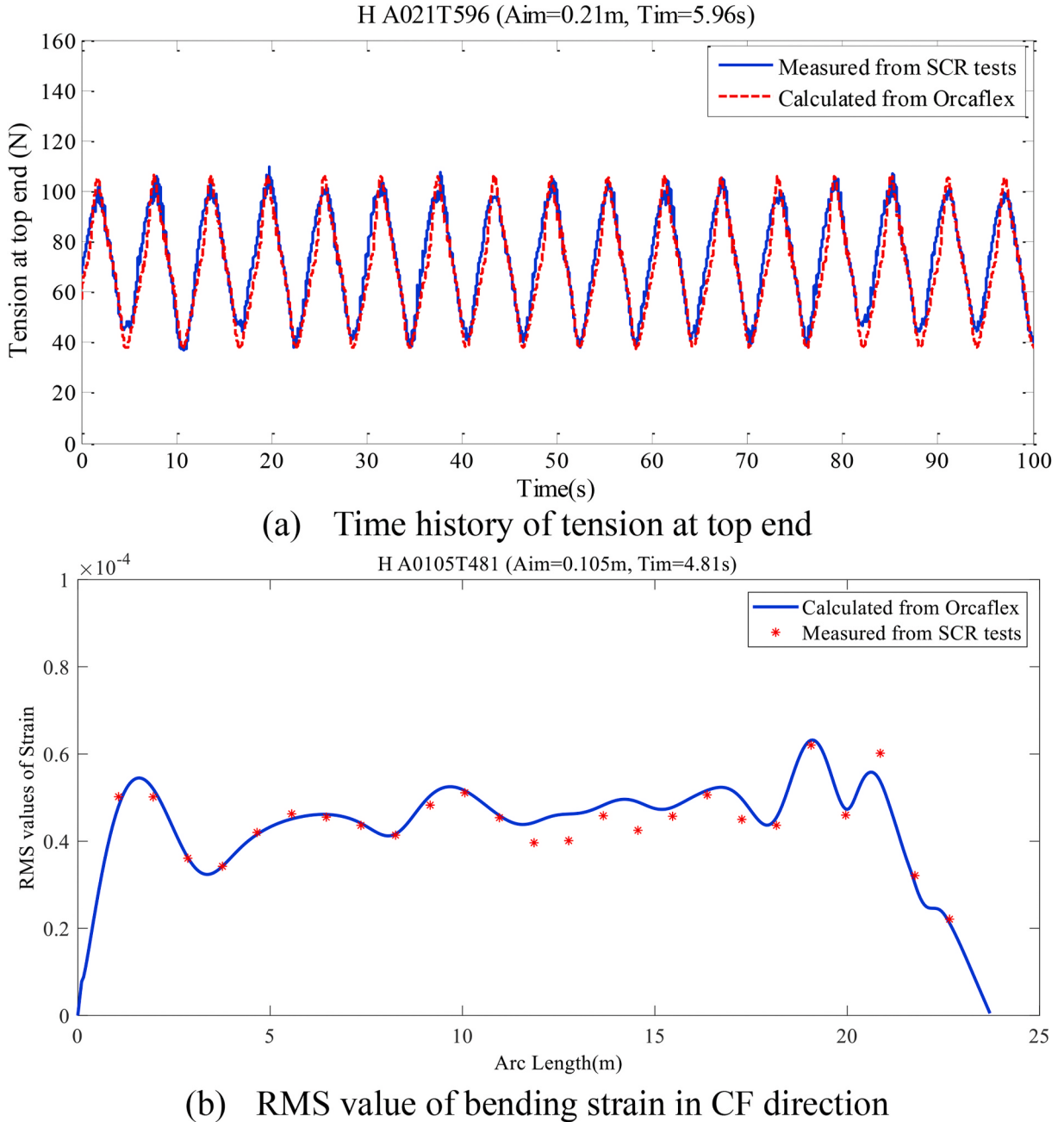


Fig. 9. Axial distributions of the measured and calculated dynamic responses (Case H A021T596).

$$f_{CF}(x, t) = \frac{1}{2} \rho D U^2(x, t) C e(x, t) \frac{\dot{y}(x, t)}{|y(x, t)|} - \frac{\rho \pi D^2}{4} C a(x, t) \ddot{y}(x, t), \quad (3)$$

where $|y(x, t)|$ represents amplitude of velocity obtained by Hilbert-Huang Transform (HHT). Fig. 2 shows time histories of velocity at one node in the SCR test and well identified time-varying amplitude by HHT. $U(x, t)$ is the relative oscillatory flow caused by the in-plane motion of SCR, which can be well reconstructed by the generalized motion reconstruction method proposed by Wang et al. [30].

The obtained coefficients $C e(x, t)$, $C a(x, t)$ in Eq. (3) will not change over time when VIV contain only one single frequency response [31], and the corresponding definition of hydrodynamic coefficients are consistent with the hydrodynamic coefficients defined by Gopalkrishnan [15]; Wu et al. (2011), and Song et al. [19].

Then the Forgetting Factor Least Squares method (FF-LS) [31–33] is employed to identify the time-varying vortex-induced force coefficients in Eq. (3). This method introduces a forgetting factor that divides the time history of the sampling data into different

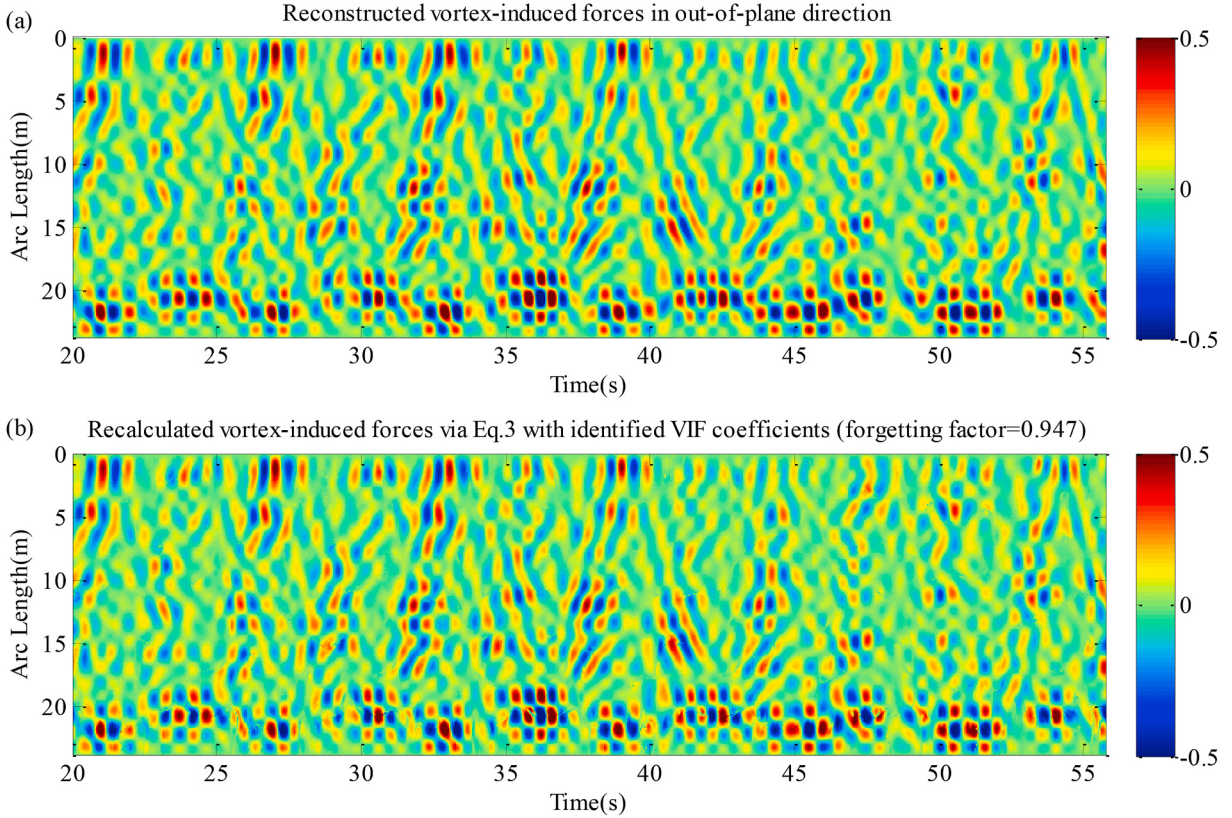


Fig. 10. Reconstructed and fitting vortex-induced forces in out-of-plane direction for Case H A0105T596, $A_{im} = 0.105$ m, $T_{im} = 5.96$ s with forgetting factor of 0.947.

regions and assigns a greater weight to the data close to the present moment. This modification improves the sensitivity of the Least Squares method and makes it possible to identify the time-varying parameters. Besides, using previous historical moments data in vortex-induced force identification also respects the dynamics nature of both fluids and structures and it may be possible to capture the memory effects.

In Eq. (3), the time-varying coefficients matrix $\theta(s)$ at the moment t_s , the time history matrix of force f_s and response H_s can be expressed as:

$$\theta(s) = \begin{bmatrix} \frac{\rho D U^2(x, t_s)}{2|\dot{y}(x, t_s)|} Ce(x, t_s) \\ -\frac{\rho \pi D^2}{4} Ca(x, t_s) \end{bmatrix}$$

$$f_s = [f_{CF}(x, t_1), f_{CF}(x, t_2), f_{CF}(x, t_3), \dots, f_{CF}(x, t_s)]^T$$

$$H_s = [\mathbf{h}(1), \mathbf{h}(2), \mathbf{h}(3), \dots, \mathbf{h}(s)]^T = \begin{bmatrix} \dot{y}(x, t_1), \ddot{y}(x, t_2), \ddot{y}(x, t_3), \dots, \ddot{y}(x, t_s) \\ \ddot{y}(x, t_1), \ddot{y}(x, t_2), \ddot{y}(x, t_3), \dots, \ddot{y}(x, t_s) \end{bmatrix}^T$$

$$s = 1, 2, 3, \dots$$
(4)

In the above equation, the initial moment and the present moment are denoted as t_1 and t_s , respectively. $t_1, t_2, t_3, \dots, t_s$ represents sampling time. f_s is the vortex-induced force at node x from the initial moment t_1 to the present moment t_s , H_s is the time history of velocity and acceleration at node x from initial moment t_1 to present moment t_s , $\theta(s)$ is dimensional vortex-induced force coefficients at node x at moment t_s . Only using the data at current moment cannot provide a unique solution for the estimation of the time-varying hydrodynamic coefficients. At a specific moment, there are two unknown variables in equation (3), but we only know one relation between these variables, i.e., equation (3). This requires us to at least use a series of measurements data for the estimation and an intuitive choice is using all data in previous measurements, which has a close relation to a widely used method based on the least squares method; e.g., Song et al. [19].

Identification of time-varying hydrodynamics can be written as identifying the time history of a set of parameters $\theta(s)s = 1, 2, 3, \dots$, which satisfy:

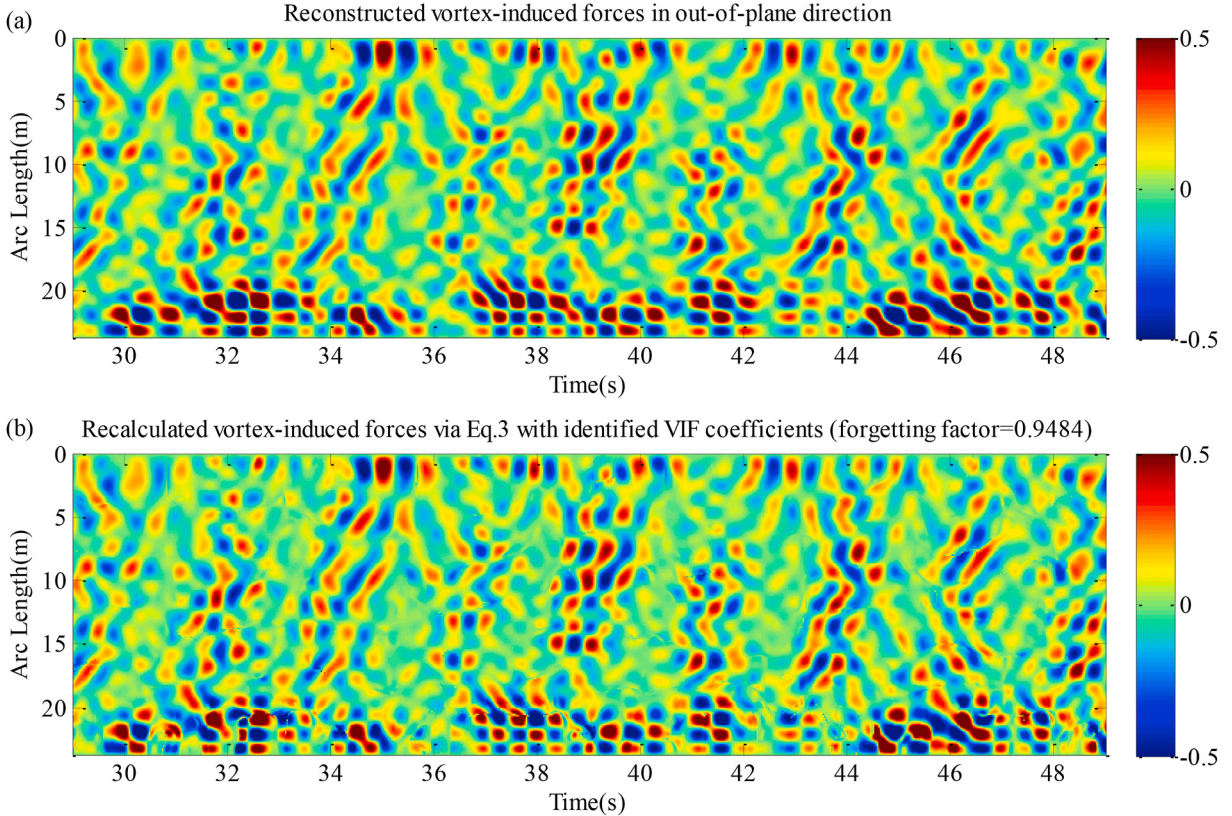


Fig. 11. Reconstructed and recalculated vortex-induced forces in out-of-plane direction for Case H A0105T481, $A_{im} = 0.105$ m, $T_{im} = 4.81$ s with forgetting factor of 0.948.

$$\mathbf{f}_s = \mathbf{H}_s \boldsymbol{\theta}(s) s = 1, 2, 3, \dots \quad (5)$$

Eq. (4) shows all previous historical moments data before t_s are used to identify time-varying parameter $\boldsymbol{\theta}(s)$.

The sampled force and response at different moments are multiplied by different data weights β , and the data weight is bigger if the data is closer to the present moment t_s . Specifically, data weight of the present moment t_s is $\beta^0 = 1$, data weight of the initial moment is β^{s-1} (β is a constant, which satisfies $0 < \beta \leq 1$). The force with data weight multiplied is:

$$\mathbf{f}_s^* = [\beta^{s-1} \mathbf{f}_s(1), \beta^{s-2} \mathbf{f}_s(2), \dots, \beta^1 \mathbf{f}_s(s-1), \beta^0 \mathbf{f}_s(s)]^T \quad (6)$$

The same weighting process is applied to the sampled response:

$$\mathbf{H}_s^* = [\beta^{s-1} \mathbf{h}^T(1), \beta^{s-2} \mathbf{h}^T(2), \dots, \beta^1 \mathbf{h}^T(s-1), \beta^0 \mathbf{h}^T(s)]^T \quad (7)$$

Therefore, Eq.(4) is rewritten as follows:

$$\mathbf{f}_s^* = \mathbf{H}_s^* \boldsymbol{\theta}(s) \quad (8)$$

According to the basic principle of Least Square method [34], the parameters to be identified need to minimize the sum of squared errors between $\mathbf{H}_s^* \boldsymbol{\theta}(s)$ and \mathbf{f}_s^* , namely:

$$\min J(\boldsymbol{\theta}(s)) = (\mathbf{f}_s^* - \mathbf{H}_s^* \boldsymbol{\theta}(s))^T (\mathbf{f}_s^* - \mathbf{H}_s^* \boldsymbol{\theta}(s)) \quad (9)$$

Solution for above Eq. (9) is:

$$\hat{\boldsymbol{\theta}}(s) = (\mathbf{H}_s^{*T} \mathbf{H}_s^*)^{-1} \mathbf{H}_s^{*T} \mathbf{f}_s^* \quad (10)$$

if $\mathbf{H}_s^{*T} \mathbf{H}_s^*$ is not a singular matrix. Substituting equations (6) and (7) into equation (10), we get:

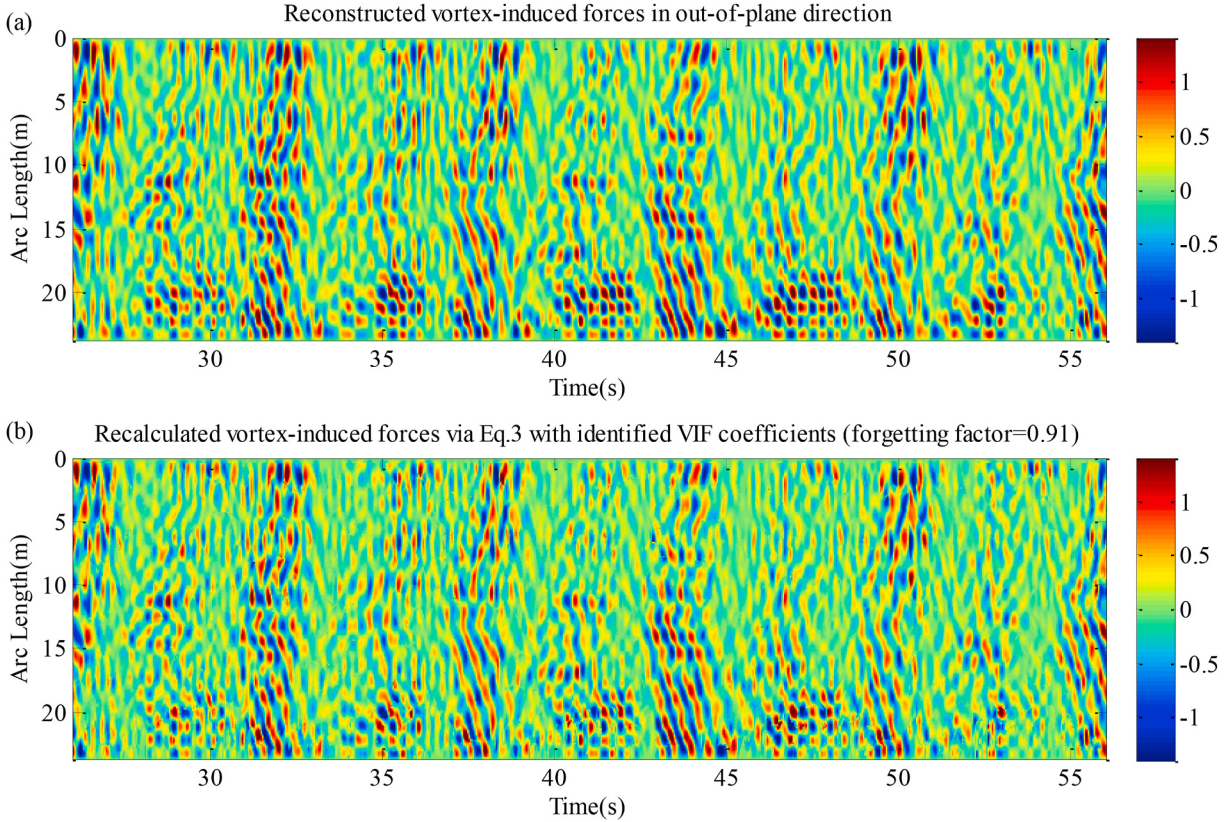


Fig. 12. Reconstructed and recalculated vortex-induced forces in out-of-plane direction for Case H A021T596, $A_{im} = 0.21$ m, $T_{im} = 5.96$ s with forgetting factor of 0.91.

$$\begin{aligned}\widehat{\boldsymbol{\Theta}}(s) &= \left[\sum_{i=1}^s \beta^{2(s-i)} \mathbf{h}(i) \mathbf{h}^T(i) \right]^{-1} \left[\sum_{i=1}^s \beta^{2(s-i)} \mathbf{h}(i) f_{CF}(x, t_i) \right] \\ &= \left[\sum_{i=1}^s \mu^{(s-i)} \mathbf{h}(i) \mathbf{h}^T(i) \right]^{-1} \left[\sum_{i=1}^s \mu^{(s-i)} \mathbf{h}(i) f_{CF}(x, t_i) \right] \\ &= (\mathbf{H}_s^T \boldsymbol{\Lambda}_s \mathbf{H}_s)^{-1} \mathbf{H}_s^T \boldsymbol{\Lambda}_s \mathbf{f}_s,\end{aligned}\quad (11)$$

where $\mu = \beta^2$, $0 < \mu \leq 1$, μ is called Forgetting Factor, $\boldsymbol{\Lambda}_s$ is the weighted matrix, whose diagonal elements are $\Lambda(s) = 1\Lambda(k-1) = \mu\Lambda(k)$, and off-diagonal elements is 0. The essence of this method is to give different weights to the data, the farther away from the present moment of data, the smaller the weight, as shown in Fig. 3:

When setting the forgetting factor $\mu = 1$, this method is equivalent to the least squares method, where equal weights are assigned to all sampled data. Different from the band pass filter employing a finite window in the frequency domain, the effect of a forgetting factor $\mu < 1$ is similar to setting a finite window in the time domain. Data far away from the current instant are associated with negligible weights (~ 0), and they can be viewed as outside of this finite window. As a result, this method is closely related to the moving least squares or local regression [35,36]. In addition, this idea of setting a finite window can be used to extend the spectral analysis using short-time Fourier analysis [37]. Different from methods with a finite window where a hard cutoff is employed, the forgetting factor in this FF-LS provides a soft cutoff on older data, and all of these approaches are effective in capturing the time-varying dynamics [38].

Although here we are processing data offline and it is possible to use the measurements at future moments, only using the data at previous time history paves the way for future application such as time-domain prediction and real-time (online) estimation. Using the measurements at previous moments further allows us to obtain the solution of Equation (11) recursively through updating the estimation with the newest measurement to save memory and speed up the computation; see e.g., Chapter 3 of Spall (2003) and Appendix A of Liu et al. (2020) for further detail. Such a recursive estimation is well established and widely used in adaptive signal processing, adaptive control, and stochastic optimization, e.g., Chapter 3 of Spall (2003).

3. SCR model test

The model test [24] was carried out in the ocean basin at Shanghai Jiao Tong University. The goal of the model test was to

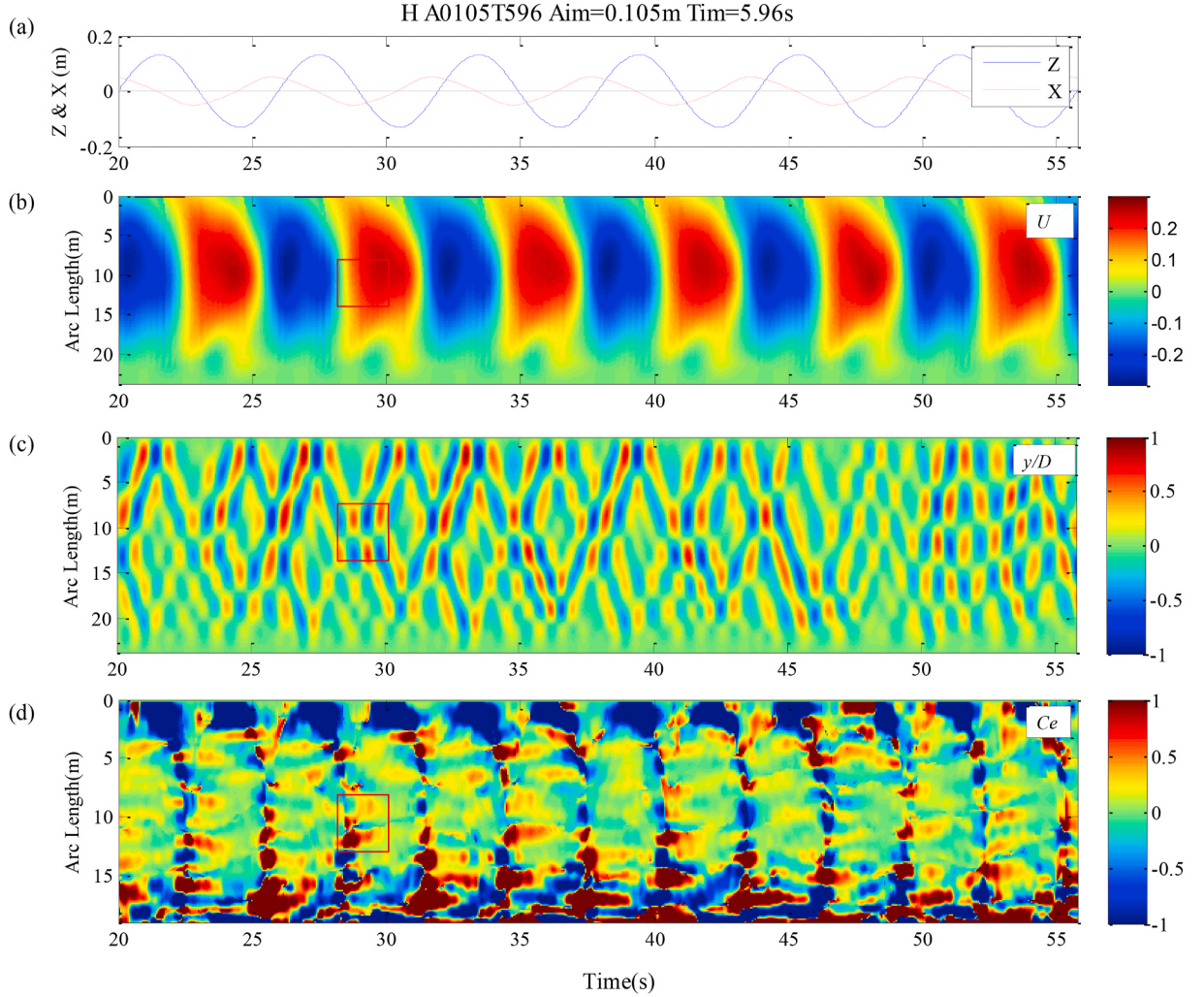


Fig. 13. (a) Time history of imposed in-plane vessel motion; (b) in-plane velocity U ; (c) non-dimensional displacement y^* ; (d) excitation coefficient C_e ; forgetting factor $\mu = 0.947$; the red frame marked an excitation region of VIVs. (Case H A0105T596, $A_{im} = 0.105$ m, $T_{im} = 5.96$ s). (For interpretation of the references to color in this figure legend, the reader is referred to the Web version of this article.)

investigate VIV effects caused by in-plane vessel motion.

Fig. 4 illustrates the overview of the experimental setup in air during the shakedown test. During the real test, the SCR model was submerged in water. The experimental setup includes two parts: one is the underwater section including a stainless-steel plate on top of a horizontal motion-controlled track, which is used to support the flow line of the SCR and to simulate the rigid seabed; the other part is the top motion section attached to the bottom of the sub-carriage. The top motion section consists of one vertical motion-controlled track on top of one horizontal track, therefore, it is able to simulate any given planar vessel motion trajectories. The SCR model was pinned connected to both the underwater and top motion systems through universal joints. Detailed description about the experimental setup can be found from published literature [6].

The SCR model is truncated due to water depth limitation in this test. The truncated SCR consists of the riser segment in the bottom sag-bend and part of the flow-line. A detailed design procedure can refer to published literature [6]. The test model was constructed with an outside coating, polypropylene random (PPR) pipe and cooper cable inside. Key parameters for SCR test model are listed in Table 1.

During the model test, top and bottom axial tension are measured using force transducers installed at ends of the model. Twenty-five evenly-distributed measuring stations, as marked in Fig. 5, are chosen to instrument the Fiber Bragg Grating (FBG) strain sensors for recording structural dynamic responses. More specifically, FBG strain sensors are divided into four groups at each measuring station, two for the in-plane and another two for the out-of-plane responses. Motion trajectories of the forced vessel motion are recorded by encoders. All the measurements are sampled synchronously with the sampling frequency at 250Hz.

In this paper, various cases with two different vessel heave motion amplitudes and two different heave motion periods are chosen to investigate the features of vessel motion-induced VIV force coefficients in out-of-plane direction. Detailed test case parameters are

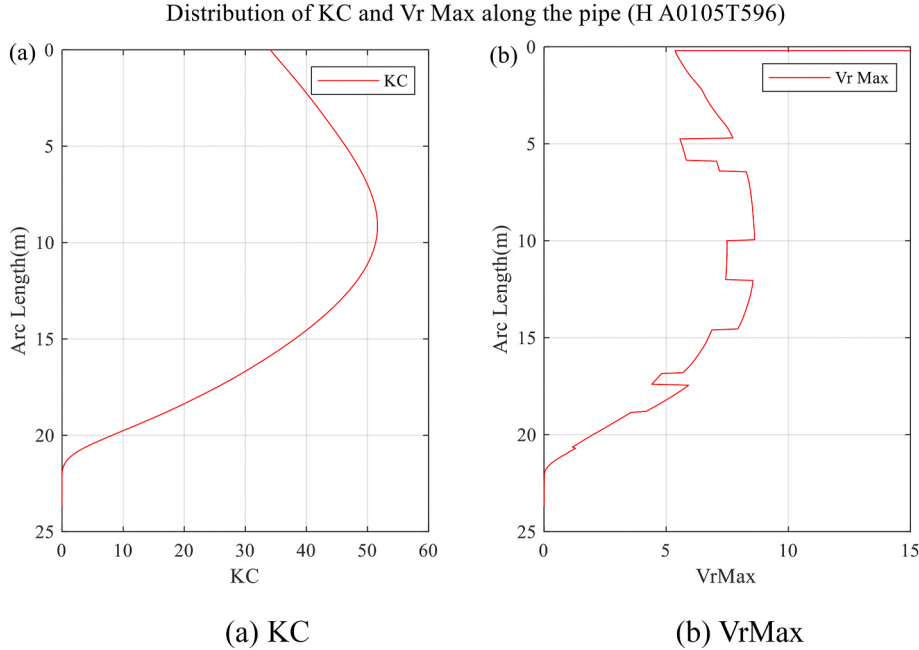


Fig. 14. Distribution of KC and $V_{r\text{Max}}$ along the pipe (H A0105T596).

listed in Table 2. Note that the heave motion parameters presented here are of the motions applied at the top of scaled model, not on the truncated model. The real applied vessel motions on the truncated model are slightly different. Detailed time histories can be found in Figs. 7–9 in Section 5. For detailed descriptions on the scaled model and truncated model, readers can refer to the published literature of Wang et al., [6].

Before vortex-induced force identification, a band-pass filter with a low-pass frequency set at four times the top forced motion frequency coupled with high-pass frequency at 50 Hz were used only on measured strains to eliminate noise at both the forced motion frequency and high frequencies. No other band pass filtering was applied. Other pre-processing of test data can be found in the published literature [6].

4. Verification of hydrodynamics identification method

The two outputs of the hydrodynamics identification method are the reconstructed forces and the identified force coefficients. In this section, to verify the reconstructed hydrodynamic force in this study, a forward FE analysis was applied by a well-validated commercial code Orcaflex [25]. Three representative test cases, H A0105T481, H A0105T596, and H A021T596, which refer to small and relatively large vessel motions are chosen to perform this verification.

The time histories of the reconstructed forces in Eq. (1) were applied on a nonlinear FE model of SCR in Orcaflex, and the vessel motions measured in the tests were treated as boundary conditions of the SCR model. Fig. 6 shows a typical time history of reconstructed forces applied at one section and the forced vessel motions at top end of SCR. It is stated that the applied forces on each node of the SCR numerical model are equivalent concentrated forces and moments of the reconstructed VIF distributed on the adjacent two elements of each node.

Tension variation has a nonnegligible effects on dynamic responses calculation of SCRs. It is mainly determined by drag forces in the in-plane direction. In the forward FE analysis, drag coefficients recommended by Wang et al. (2019) are adopted, which represent a combination of the different drag coefficients 1.3, 1.6 and 1.9 for segments of bottom end to sensor location 8, sensor location 8 to 15, and sensor location 15 to top end, respectively. Figs. 7(a)–9(a) present a comparison between the simulated and measured top tensions. As can be observed in this figure, the simulated tension variations from Orcaflex agree well with the measured values.

The Dynamic responses including CF displacements and bending strains are calculated via the numerical integration method in Orcaflex [25]. Comparisons between the simulated and measured RMS values of CF bending strains are provided in Figs. 10–12. It can be found that the simulated results basically coincide with the measured results, which demonstrates validity of the identified vortex-induced forces in this paper.

The accuracy of identified coefficients via FF-LS is influenced by forgetting factors [31]. In this study, we adjusted forgetting factors for each case to ensure that the mean relative squared error between the reconstructed forces by Eq. (1) and the fitting forces in Eq. (3) by FF-LS is smaller than 10%. Figs. 10–12 present the reconstructed forces by Eq. (1) and the fitting forces in Eq. (3) by FF-LS. It can be easily found that the fitting forces by FF-LS agree well with the reconstructed forces, which demonstrates the validity of the identified hydrodynamic force coefficients in this paper.

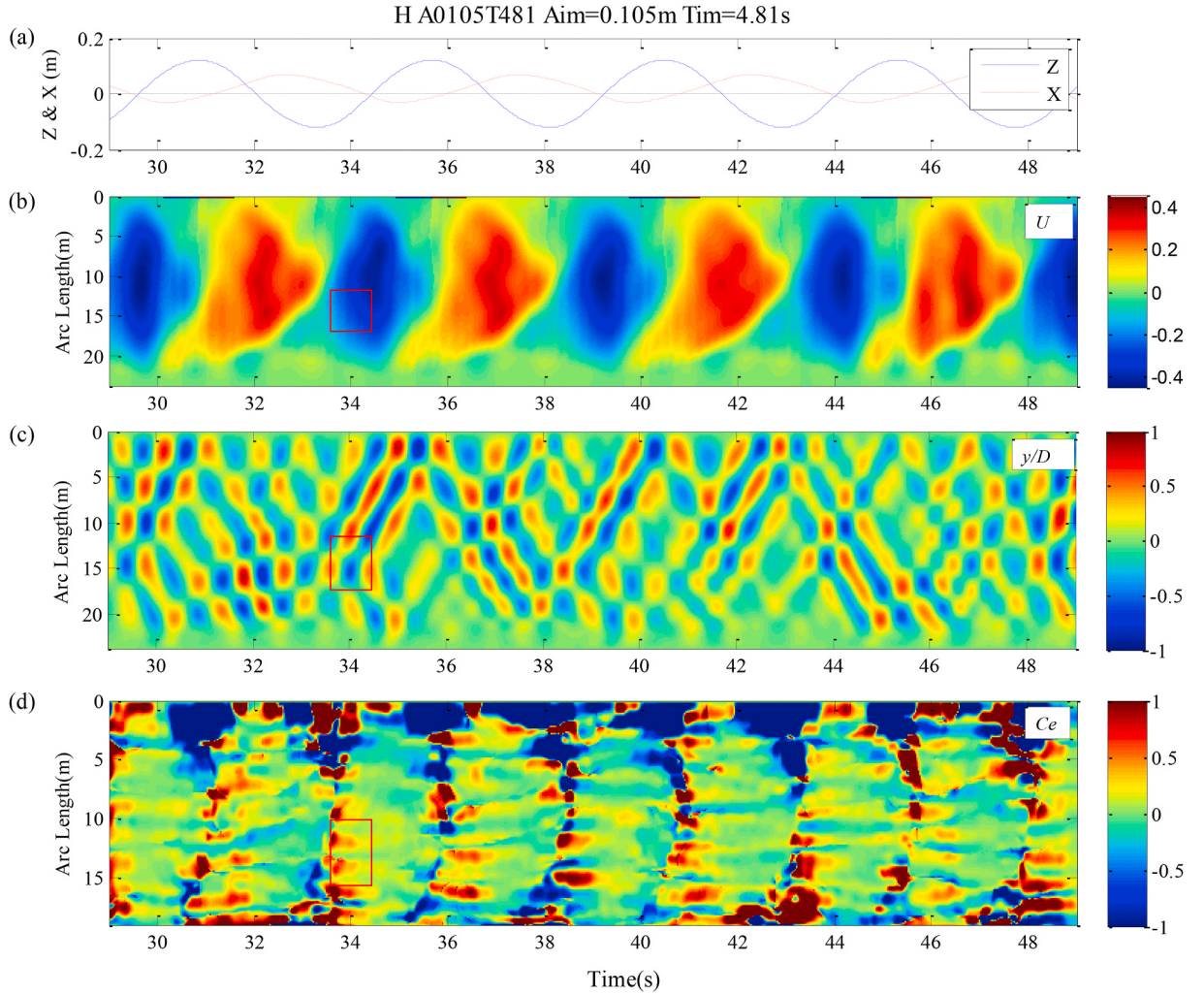


Fig. 15. (a) Time history of imposed in-plane vessel motion; (b) in-plane velocity U ; (c) non-dimensional displacement y^* ; (d) excitation coefficient C_e ; forgetting factor $\mu = 0.945$; the red frame marked an excitation region of VIVs. (Case H A0105T481, $A_{im} = 0.105$ m, $T_{im} = 4.81$ s). (For interpretation of the references to color in this figure legend, the reader is referred to the Web version of this article.)

5. Hydrodynamic results and discussion

In present section, three test cases with two different heave motion amplitudes (0.105 m and 0.21 m) and two periods (4.81 s and 5.96 s) are selected to investigate spatial-temporal distribution of VIV responses, and vortex-induced force coefficients including excitation coefficients and added mass coefficients. Detailed parameters of the three cases are listed in Table 2.

Reynolds number Re , non-dimensional tension variation T_r , KC number, the max reduced velocity Vr_{max} and non-dimensional displacement y^* used in following discussions are calculated based on the definitions in Eq. (12):

$$\begin{aligned} Re(x, t) &= \frac{U(x, t)D}{\nu}, \quad T_r(x, t) = \frac{T(x, t)}{T_{pre,top}}, \quad KC(x) = \frac{2\pi A_{IL}(x)}{D}, \\ Vr_{max}(x) &= \frac{\sqrt{2}U_{rms}(x)}{f_d(x)D}, \quad y^*(x, t) = \frac{y(x, t)}{D}, \end{aligned} \quad (12)$$

where $U(x, t)$ and $A_{IL}(x)$ are the in-plane velocity and in-plane displacement amplitude of location x , which are reconstructed from measured in-plane strain signals by the reconstruction method proposed by Wang et al. Wang et al. [30]; $U_{rms}(x)$ is the RMS value of in-plane velocity; $f_d(x)$ is the dominant frequency of VIV displacements at location x , which is a constant value for each node and obtained by Fast Fourier Transform (FFT). ν is the kinematic viscosity of fluid; D is the outer diameter of SCR; and $T_{pre,top}$ is the pre-tension at the top end of SCR, which is measured in model tests.

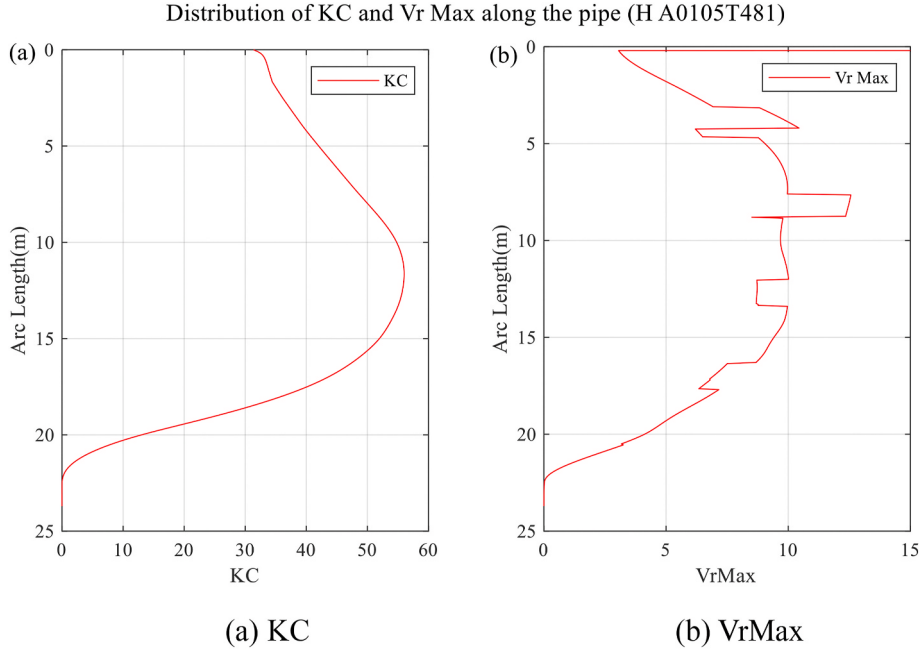


Fig. 16. Distribution of KC and $V_{r\max}$ along the pipe (H A0105T481).

5.1. Spatial-temporal distribution of excitation coefficients

Figs. 13–15 present time histories of imposed vessel motion at the top end of SCR, spatial-temporal distribution of in-plane velocity U , non-dimensional displacement y^* , and the excitation coefficient Ce for the three cases (H A0105T596, H A0105T481 and H A021T596). As illustrated in subgraph (b), the in-plane flow field of SCR is a type of sheared-oscillatory flow, whose largest flow velocity are located at the middle part of SCR. With the increase of vessel motion velocity, higher modes of VIV responses are excited due to the larger in-plane flow velocities.

It can be observed from the subgraphs (d) of Figs. 13, 15 and 17 that when the in-plane relative flow changes direction, there are unnegligible fluctuations of the excitation coefficients, whose values are greater than 1 or smaller than -1. A similar phenomenon was also found in in-plane drag force [39]. The main reason for this phenomenon is that when the relative flow in in-plane changes direction, the pipe reverses to its own wake, which brings disordered in-coming flow on the pipe, further leading to fluctuated loads and excitation coefficients. The duration of this phenomenon is around 20% of half a vessel motion period. Except for this duration, most of the excitation coefficients on segments from 3 m to touch down point vary from -0.2 to 0.5. As expected, traveling wave starts at the middle part of the pipe (red rectangle in Figs. 13, 15 and 17), where relative flow velocity and KC number (Figs. 14, 16 and 18) are the largest at that region and the corresponding max reduced velocities $V_{r\max}$ are around 7 to 10, as shown in Figs. 14, 16 and 18; and correspondingly, the excitation coefficients of this region are almost positive.

Furthermore, it is noticed that there is a damping region at the top end of SCR, which may result from the reflecting wave breaking the lock-in between vortex-shedding and pipe vibration. The excitation coefficients on the flow line segment (from around 14 m to the end of SCR) have an extremely large absolute value. This is due to the fact that the definition of excitation coefficients in Eq. (3) has a value close to zero in the denominator when flow velocity is close to zero. Similar phenomena had also been reported by Wu et al. (2011) in hydrodynamic coefficients identification for VIVs under sheared flow, where the excitation coefficients were extremely larger when flow velocity was close to zero at the lower end of the pipe.

In addition, it is found from Figs. 13, 15 and 17 that most of the VIV excitation region where traveling wave starts exists in the acceleration period, while during the deceleration period, even if the relative flow velocity is same as that in acceleration period, there is no VIV excitation region. To understand this difference, the average spatial-temporal distributions of in-plane velocity and excitation coefficients during half a vessel motion period which are the mean values over 20 vessel motion periods as illustrated in Eq. (13), are obtained and provided in Fig. 16.

$$\begin{aligned} Ce_{mean}(x, t') &= \frac{1}{20} \sum_{s=0}^{19} Ce(x, t'^{+s \cdot n_T}), \\ Ca_{mean}(x, t') &= \frac{1}{20} \sum_{s=0}^{19} Ca(x, t'^{+s \cdot n_T}), \end{aligned} \quad (13)$$

$$n_T = T_{im} \cdot f_{sample},$$

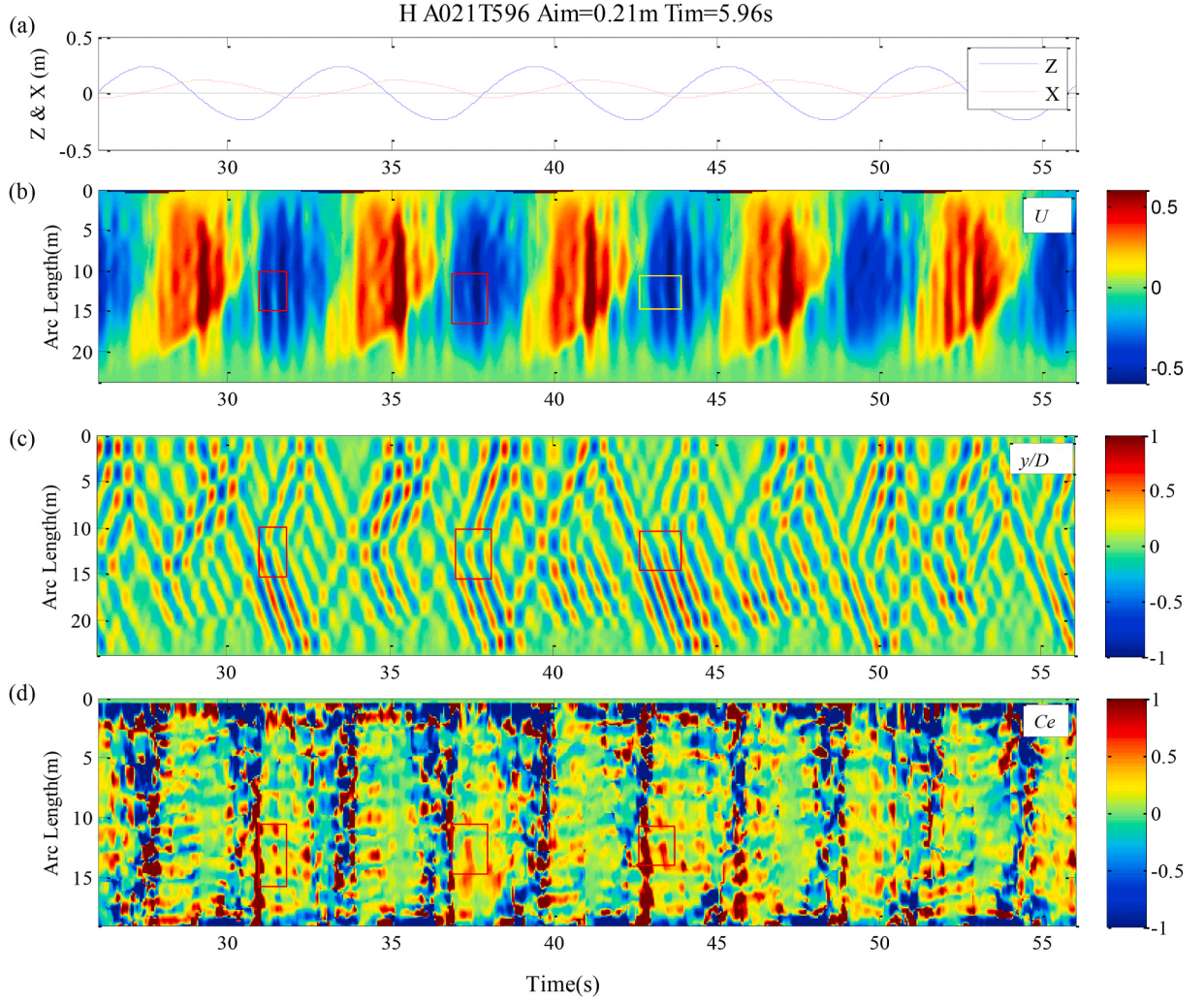


Fig. 17. (a) Time history of imposed in-plane vessel motion; (b) in-plane velocity U ; (c) non-dimensional displacement y^* ; (d) excitation coefficient C_e ; forgetting factor $\mu = 0.91$; the red frame marked an excitation region of VIVs. (Case H A021T596, $A_{im} = 0.21$ m, $T_{im} = 5.96$ s). (For interpretation of the references to color in this figure legend, the reader is referred to the Web version of this article.)

where T_{im} is the period of imposed vessel motion, and f_{sample} is the sampling frequency, which is 250Hz in this study. It can be found in Fig. 19 that when the flow velocity just begins to accelerate, there are several regions on the pipe with large excitation coefficients, and the coefficient value can reach more than 0.4. As the acceleration slows down, the value of the excitation coefficient decreases, and the values are basically maintained until the end of the deceleration. At the end of the deceleration, there are few regions where excitation coefficient gets larger. Then the differences between VIV responses characteristics in acceleration period and the deceleration period can be explained. The larger excitation coefficients (up to 0.4) at the beginning of acceleration period provide the pipe positive excitation with energy coming from fluid to the pipe, resulting obvious vibration. Then, vibration waves travel to the other part of the pipe and this excitation energy is dissipated by traveling wave radiation damping. While in the deceleration period, even there are some regions with positive coefficients, but they are too small to excite obvious VIVs. Reasons of the excitation coefficients differences in acceleration and deceleration period may be that the vortex shedding did not follow up the change of velocity, causing a lag between vortex shedding and pipe vibration with no lock-in occurring. Detailed wake visualization tests or simulations are suggested for further understanding .

To have a deeper insight of this phenomenon, parameter $\gamma(x, t) = (D / U_{max}^2(x)) \cdot (\partial U(x, t) / \partial t)$, which considers the relative significance of the local acceleration to the convective acceleration, is introduced. $U_{max}(x)$ is the maximum value of in-plane velocity at location x . If γ is small [1] the flow may be approximated by a juxtaposition of steady states; i.e., by flows with negligible or no history effects. Its positive and negative values represent acceleration and deceleration, respectively. In Fig. 20, distributions of excitation coefficients over γ and real reduced velocity V_r ($V_r = U(t)/f_{dominant}(t)D$, $f_{dominant}(t)$ is the time-varying dominant frequency of VIV displacements, which is obtained by wavelet analysis) for the three cases provided. The excitation coefficients shown in this figure are

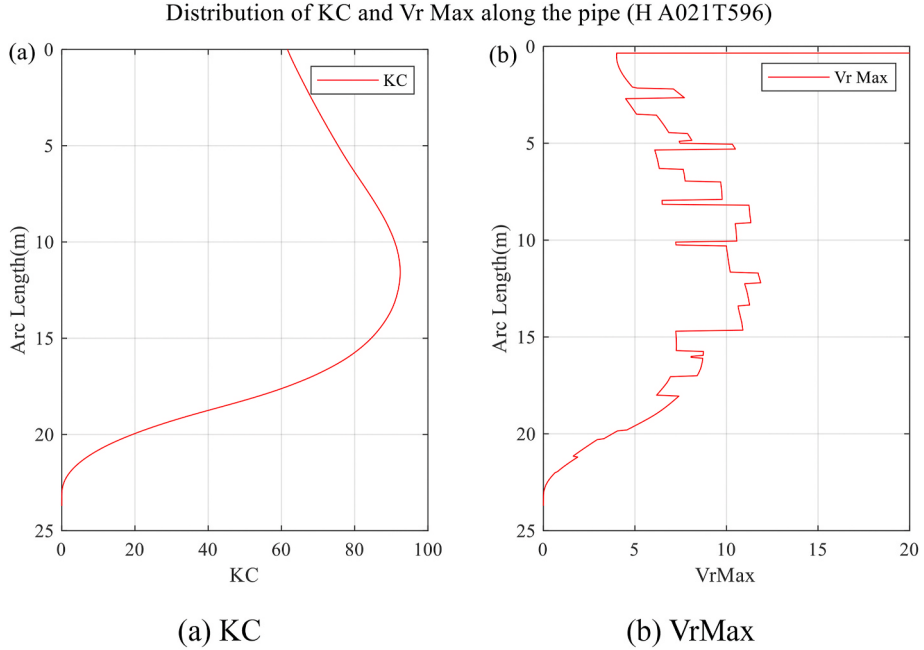


Fig. 18. Distribution of KC and $V_{r\text{Max}}$ along the pipe (H A021T596).

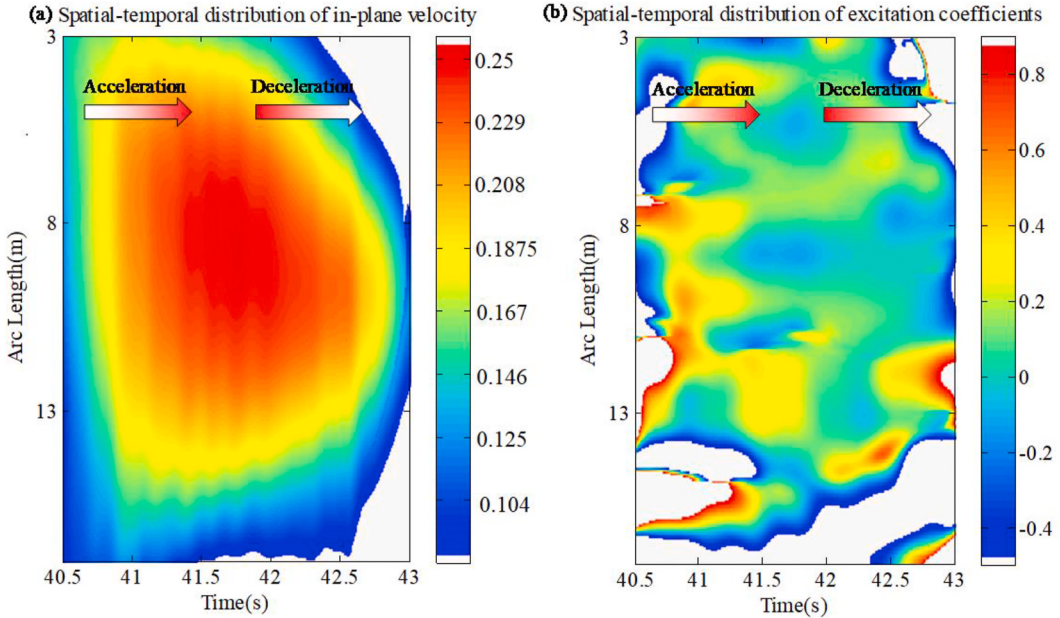


Fig. 19. (a) Spatial-temporal distribution of in-plane velocity U , (b) Spatial-temporal distribution of excitation coefficients C_e during half a vessel motion period; the presented in-plane velocity and excitation coefficients are the average values of 20 vessel motion periods (Case H A0105T596, $A_{im} = 0.105 \text{ m}$, $T_{im} = 5.96 \text{ s}$).

the mean values over 20 vessel motion periods, as shown in Eq. (13).

When time-varying reduced velocity V_r is larger than 4, differences between excitation coefficients under the acceleration period (positive γ) and the deceleration period (negative γ) are apparent in Fig. 20. That is, the excitation coefficients are approximately 0 or even negative (green to blue color in Fig. 20) when the parameter is negative. While under the condition of positive γ , there are positive excitation coefficients (yellow to red color in Fig. 20), most of which are larger than 0.2. Moreover, the closer positive γ is to 0, the larger the positive excitation coefficient value. This can be explained as the steadier the flow velocity, the easier it is to excite vortex-

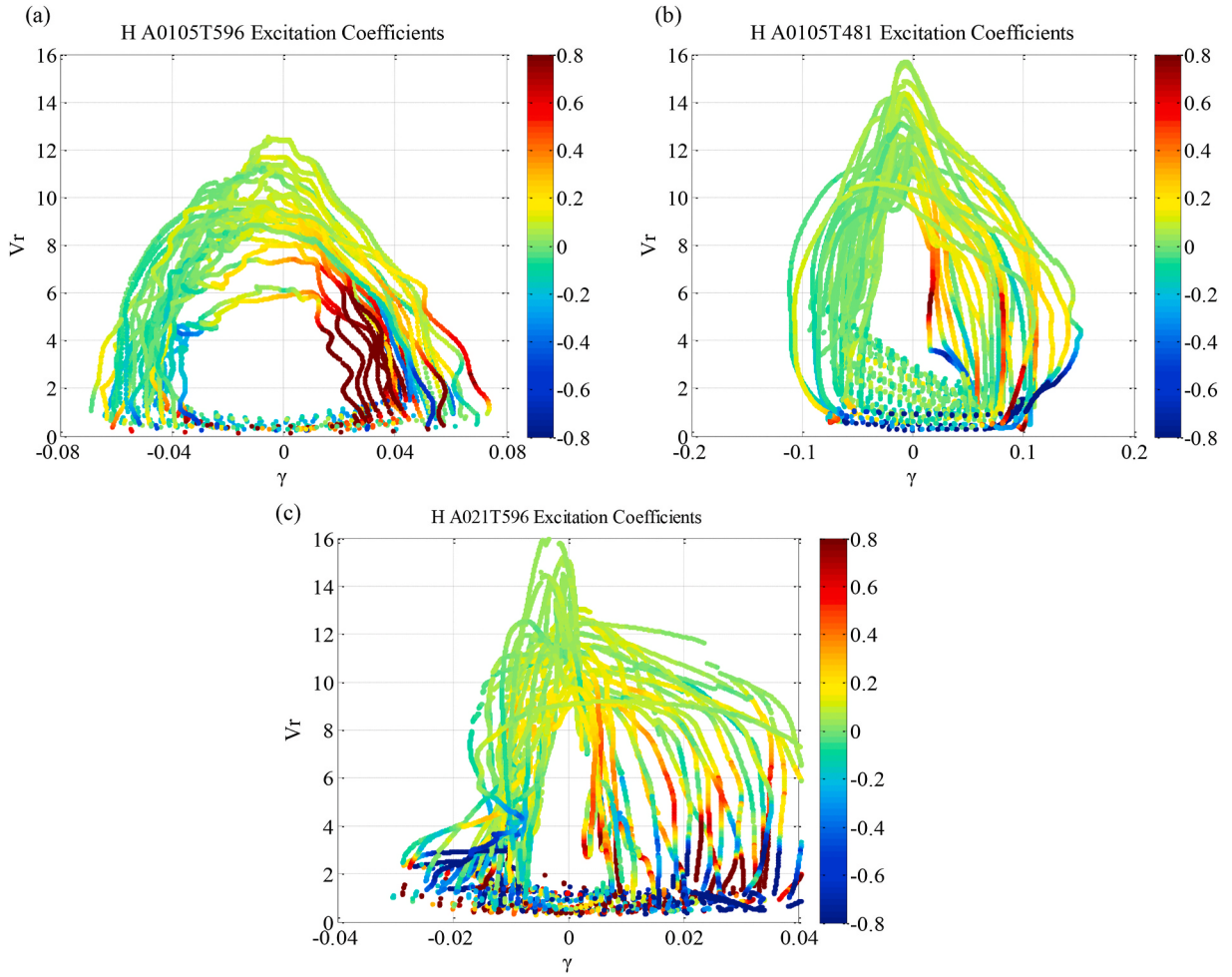


Fig. 20. Distribution of excitation coefficients over γ and V_r of 13 locations which are uniformly distributed on the segment from 3 m to 16 m of SCR: (a) Case H A0105T596, $A_{im} = 0.105$ m, $T_{im} = 5.96$ s; (b) Case H A0105T481, $A_{im} = 0.105$ m, $T_{im} = 4.81$ s; (c) Case H A021T596, $A_{im} = 0.21$ m, $T_{im} = 5.96$ s; The color represents excitation coefficient. (For interpretation of the references to color in this figure legend, the reader is referred to the Web version of this article.)

induced vibration because there is sufficient time for lock-in to occur.

However, for the three cases, the excitation coefficient values still have differences under the same V_r and γ values during the acceleration period of in-plane flow velocity. This may result from parameters that affect the excitation coefficient other than the parameters γ and V_r , such as non-dimension amplitude, amplitude variation rate, vibration frequency change, and so on. As these variables cannot be controlled in this SCR test, the specific relationship between parameter γ , V_r and the excitation coefficient cannot be given for the time being. In the future, more advanced data analysis techniques, such as machine learning methods, or more advanced experimental techniques can be used to conduct more systematic research on this issue.

5.2. Spatial-temporal distribution of added mass coefficients

Figs. 21–23 present the time history of imposed vessel motions at top end, tension variation ratio T_r , non-dimensional displacement y^* , dominant frequency, and added mass coefficient Ca of these three cases (H A0105T596, H A0105T481 and H A021T596). The dominant frequency at each node and each time step is obtained by wavelet analysis [6]. It is found that added mass coefficients of SCR varies greatly with most of the values being from -2 to 2.

When VIV responses are traveling wave dominant, the added mass coefficients are basically unchanged and are all around 1.0, as presented in the red rectangle of Figs. 21–23. Meanwhile, the dominant frequencies of traveling wave dominant VIV responses are basically consistent, especially for case H A021T596 of which the traveling wave features are evident.

In addition, the added mass coefficient has a positive correlation with tension variations when the tension varies severely. Fig. 24 provides distributions of added mass coefficients over T_r and time-varying real reduced velocity V_r for the three cases. The added mass coefficients shown in this figure are the mean values over 20 vessel motion periods as shown in Eq. (13). It can be found that the

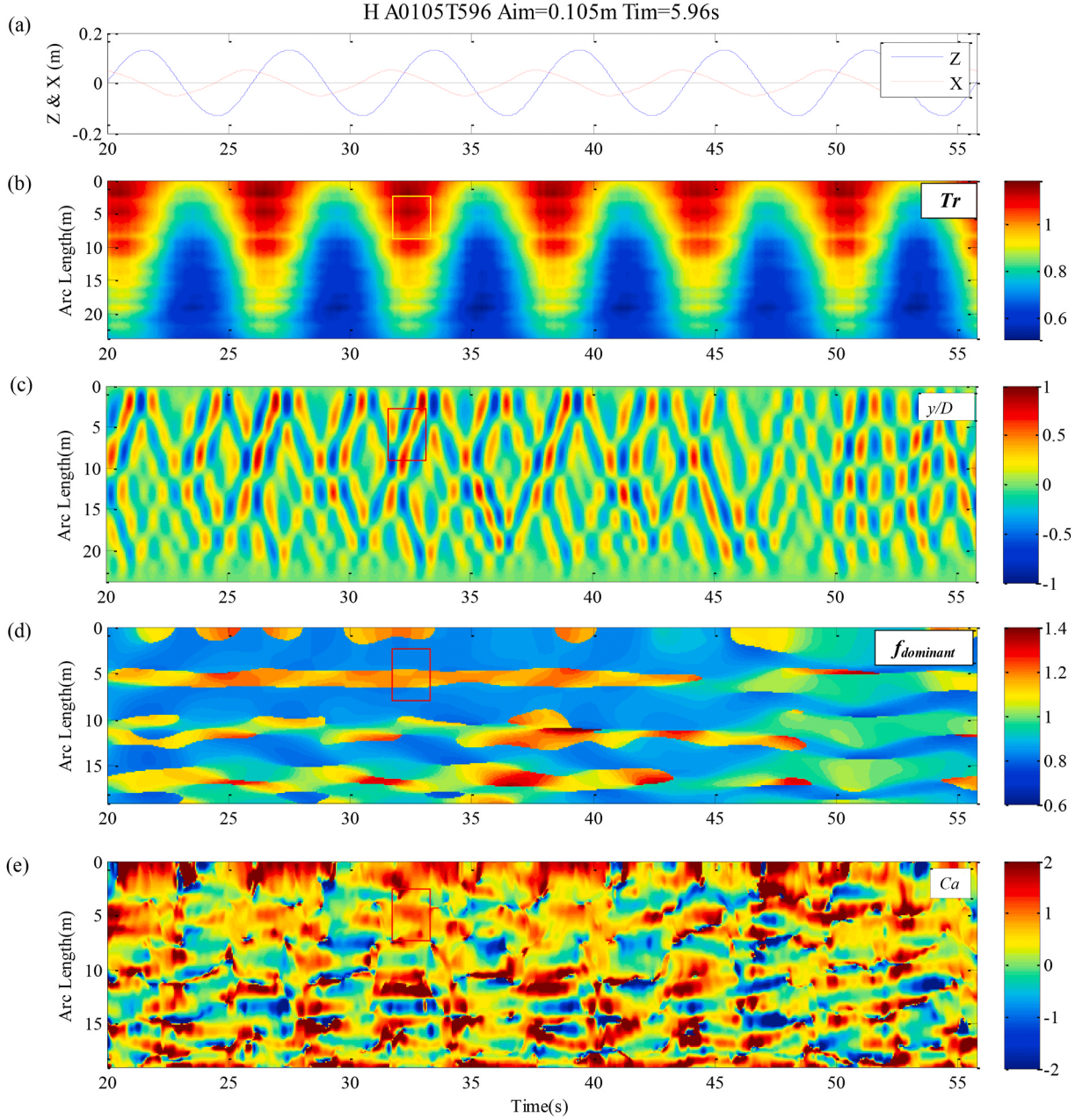


Fig. 21. (a) Time history of imposed vessel motion; (b) tension variation ratio T_r ; (c) non-dimensional displacement y^* ; (d) dominant frequency by wavelet analysis; (e) added mass coefficient Ca , forgetting factor $\mu = 0.947$; the red frame marked a traveling wave region of VIVs. (Case H A0105T596, $A_{im} = 0.105$ m, $T_{im} = 5.96$ s). (For interpretation of the references to color in this figure legend, the reader is referred to the Web version of this article.)

positive correlation between the added mass coefficient and tension variation is obvious under case H A021T596, of which tension variation ratio T_r at the top end of SCR varies from 0.4 to 1.6. Most of the added mass coefficients under case H A021T596 are larger than 0.5 (yellow to red color in the figure) when tension variation ratio T_r is larger than 0.7. While there are more negative values (green to blue color in the subplot c) of added mass coefficients when the tension variation ratio T_r is smaller than 0.7, and the closer T_r is to 0, the smaller the added mass coefficients. This phenomenon is not evident for the other two cases whose tension variation ratio at the top end of SCR is from 0.9 to 1.15 for case H A0105T596 and from 0.75 to 1.25 for case H A0105T481. The reason for this phenomenon may because of a self-modulated frequency feature of VIVs. It has been found that when SCR is subject to time-varying tension at the top end, its wet natural frequency (considering Ca) changes [40], which will break the lock-in between wet natural frequency, structural vibration, and vortex shedding if added mass coefficients Ca remain unchanged. However, the results in this

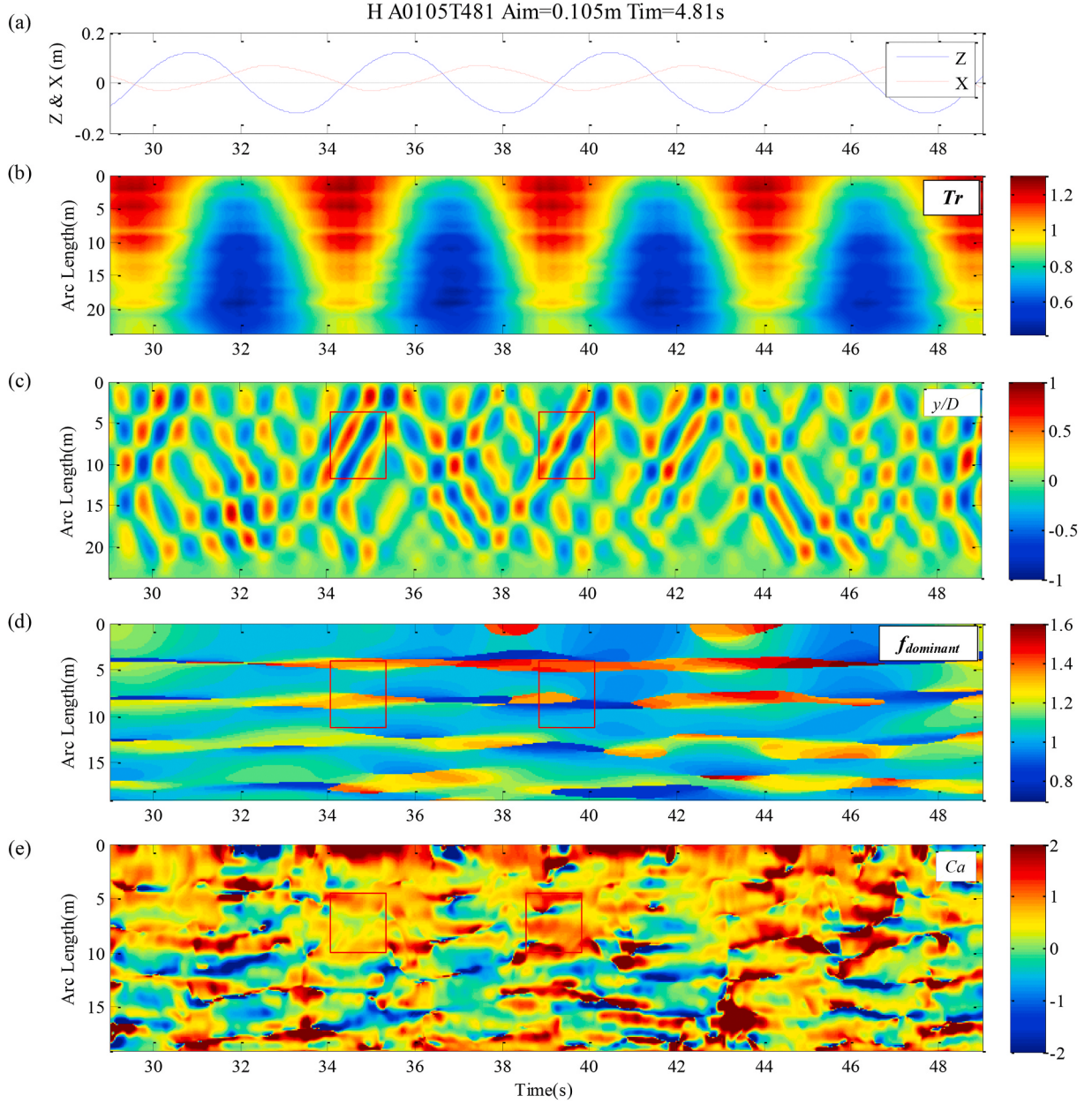


Fig. 22. (a) Time history of imposed vessel motion; (b) tension variation ratio T_r ; (c) non-dimensional displacement y^* ; (d) dominant frequency by wavelet analysis; (e) added mass coefficient Ca , forgetting factor $\mu = 0.945$; the red frame marked traveling wave regions of VIVs. (Case H A0105T481, $A_{im} = 0.105$ m, $T_{im} = 4.81$ s). (For interpretation of the references to color in this figure legend, the reader is referred to the Web version of this article.)

study show that the added mass coefficients change with the tension variations, which tends to offset the variation of natural frequency so that the lock-in can keep.

5.3. Chaotic features of VIV and VIF

A significant feature of VIV responses and excitation coefficient distributions is chaotic behavior. For case H A0105T596, it can be observed from Fig. 13 (c), the spatial-temporal distributions of VIV response at 23s–45s are not purely periodic but can be characterized as quasi-periodic. While the VIV responses at 45s–50s are basically disappeared and then have wider regions of stationary wave at 50s–55s, which are different from those at 23s–45s. With the increase of vessel motion velocity, the chaotic feature becomes more apparent. For case H A0105T481 and case H A021T596, it is almost impossible to find an oscillation period in which the spatial-

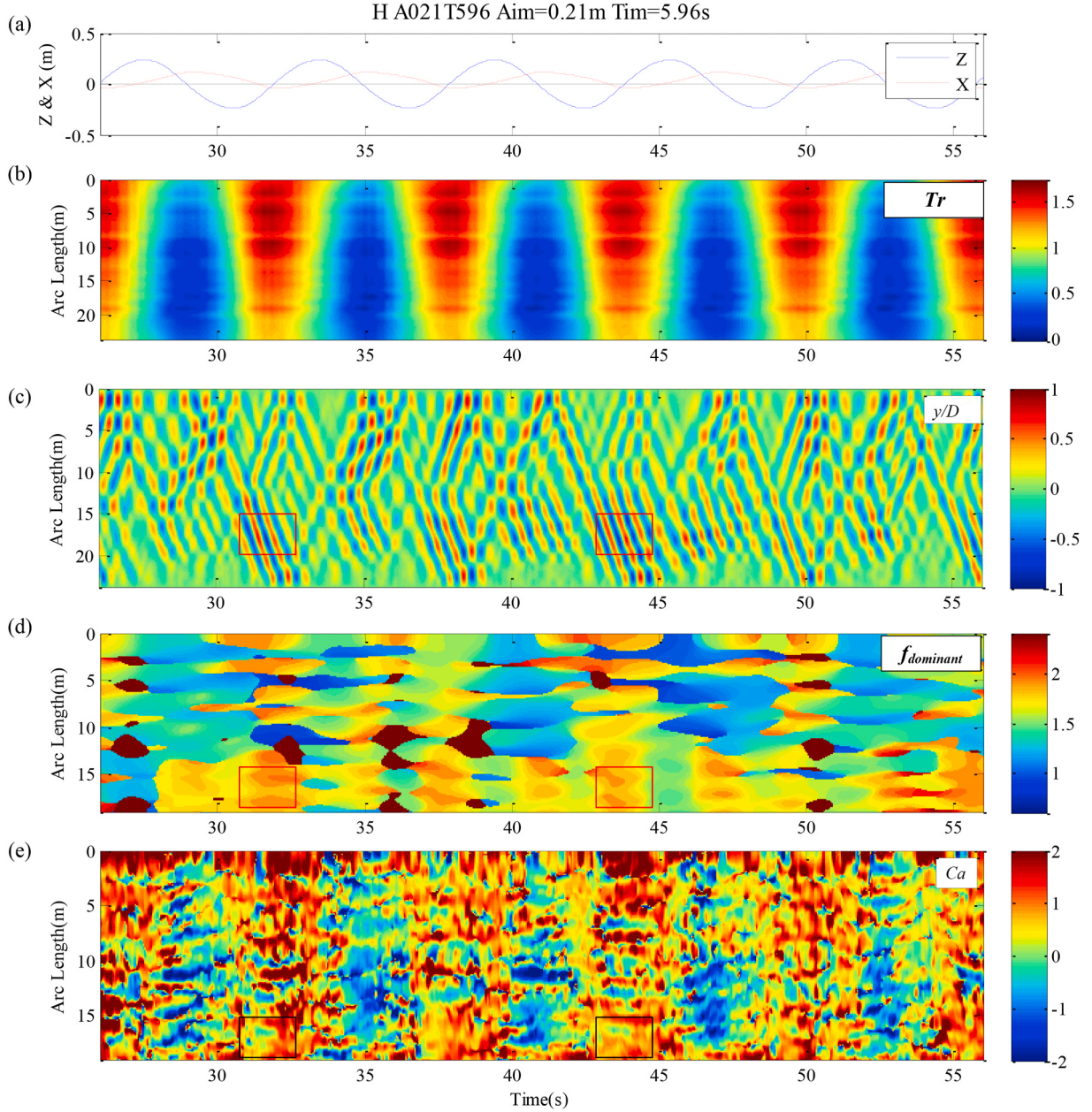


Fig. 23. (a) Time history of imposed vessel motion; (b) tension variation ratio T_r ; (c) non-dimensional displacement y^* ; (d) dominant frequency by wavelet analysis; (e) added mass coefficient Ca , forgetting factor $\mu = 0.91$; the red frame marked traveling wave regions of VIVs. (Case H A021T4596, $A_{im} = 0.21$ m, $T_{im} = 5.96$ s). (For interpretation of the references to color in this figure legend, the reader is referred to the Web version of this article.)

temporal distributions of VIV responses are the same. Similarly, there also exist chaotic behaviors for added mass coefficients, as shown in Figs. 21–23.

To qualitatively differ the chaotic behaviors versus quasi-periodic behaviors, FFT results, the phase plane [41], and the Poincaré map [42] of case H A0105T596 and H A021T596 are demonstrated in Figs. 25 and 26. Phase plane shows trajectories of the dynamical system along two state variables that are displacement and velocity for VIV of one point. The Poincaré map is an intersection of the dynamical system in the state space. Here the trigger to plot the Poincaré map is a value of zero for the cross-flow acceleration. From the phase plane and the Poincaré map, we can qualitatively analyze whether a dynamic system is periodic, quasi periodic, or chaotic. For a periodic or quasi periodic dynamical system, the trajectory on the phase plane will converge to an equilibrium line; and the corresponding Poincaré map will have several clustered points representing the number of vibration frequencies [43,48]. While for a dynamical system with chaotic behavior, the trajectories on the phase plane will be random and trend to fill up the entire region, and

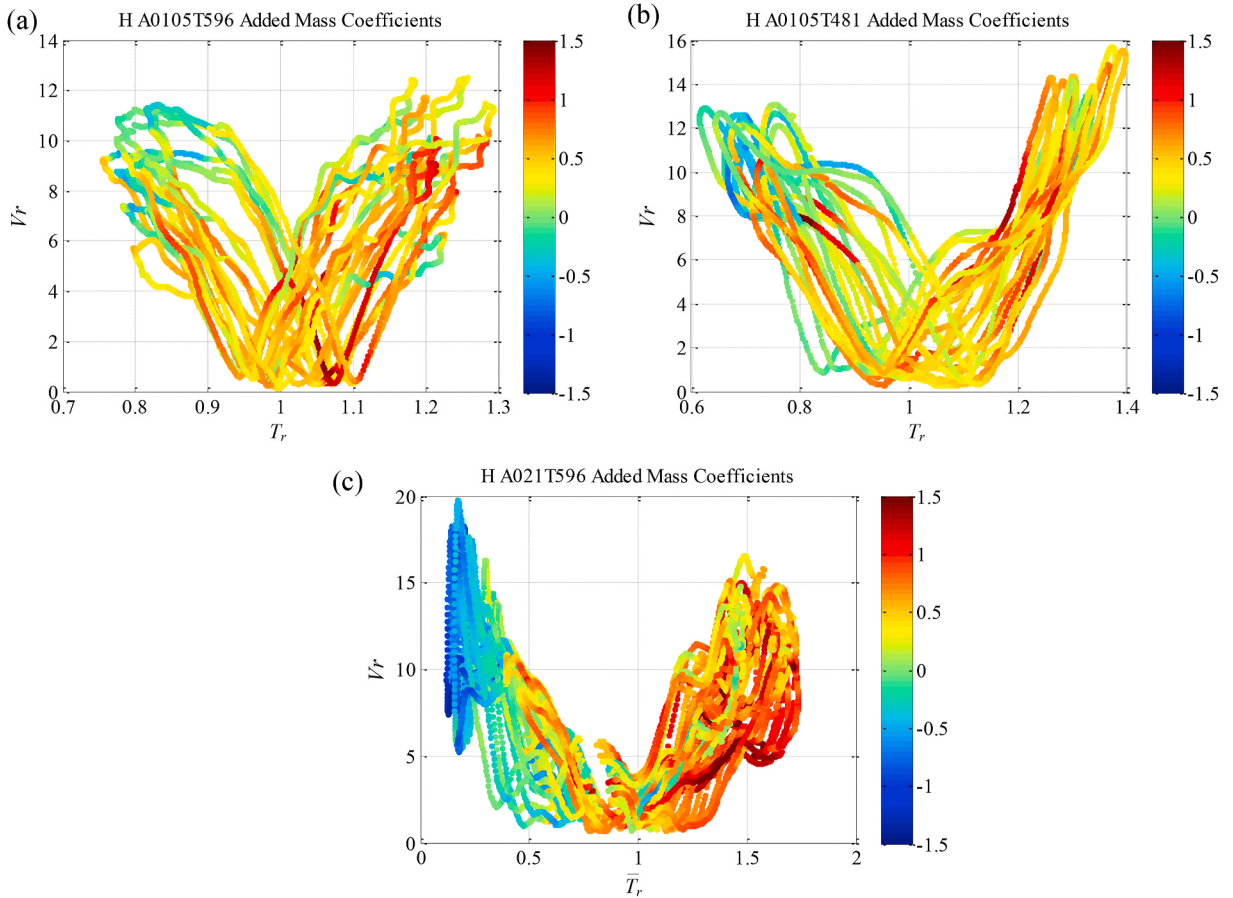


Fig. 24. Distribution of added mass coefficients over T_r and V_r of 13 locations which are uniformly distributed on the segment from 3 m to 16 m of SCR: (a) Case H A0105T596, $A_{im} = 0.105$ m, $T_{im} = 5.96$ s; (b) Case H A0105T481, $A_{im} = 0.105$ m, $T_{im} = 4.81$ s; (c) Case H A021T596, $A_{im} = 0.21$ m, $T_{im} = 5.96$ s; The color represents added mass coefficient. (For interpretation of the references to color in this figure legend, the reader is referred to the Web version of this article.)

there will be many random points on the Poincaré map.

For case H A0105T596 ($A_{im} = 0.105$ m, $T_{im} = 5.96$ s), the time history, the PSD plot, the phase plane and the Poincaré map of displacement signal from 20s to 43.84s (4 vessel motion periods) at the location of $x = 5.5$ m are provided in Fig. 25. The signal shows a dominant frequency at 1.15Hz alongside the other four small frequency peaks. Trajectories on the phase plane trend to an equilibrium cycle ring (red cycle in Fig. 25). Points on the Poincaré map are mainly clustered into two groups. This type of response is referred as quasi-periodic VIV.

For case H A021T596 ($A_{im} = 0.21$ m, $T_{im} = 5.96$ s), Fig. 26 gives the time history, the PSD plot, the phase plane and the Poincaré map of displacement signal from 28s to 52s (4 vessel motion periods) at the location of $x = 5.5$ m. There are multiple frequency components that are close and wide-broad in the PSD plot, and trajectories on the phase plane are cycles with different centers and radii. The chaotic behaviors are also evidenced by the disordered points on the Poincaré map. The majority of vessel motion-induced VIV responses for SCR present a behavior similar to those given in Fig. 26. The chaotic behavior was also found in NDP Riser High Mode VIV tests under uniform and linearly sheared flow [43,44], which was treated as a generic feature of VIV for flexible pipes.

In this study, the chaotic behavior of excitation coefficients is initially presented. It is more apparent under the case of large vessel motions. As illustrated in Fig. 27, the excitation coefficients at $x = 5.5$ m of case H A0105T596 ($A_{im} = 0.105$ m, $T_{im} = 5.96$ s) exhibit quasi-periodic behavior, while those of case H A021T596 ($A_{im} = 0.21$ m, $T_{im} = 5.96$ s) are more random. One of the main reasons for this phenomenon is that vortex-shedding is strongly coupled with in-plane motions. That is, the relative in-plane velocity will induce vortex shedding behind SCR, and VIV responses will occur when vortex-shedding frequency is close to the natural frequencies of SCR. This VIV response will further change the surrounding flow of the pipe and lead to a variation of drag force in the in-plane direction, which will result in different in-plane motions. This coupling is evidenced by the time histories of excitation coefficients and the in-plane velocity in Fig. 27(b). Randomness exists in both the excitation coefficient and the in-plane velocity for case H A021T596, while there is basically no randomness in the time histories of the excitation coefficient and the in-plane velocity for case H A0105T596, which shows the same quasi-static behavior as the VIV responses.

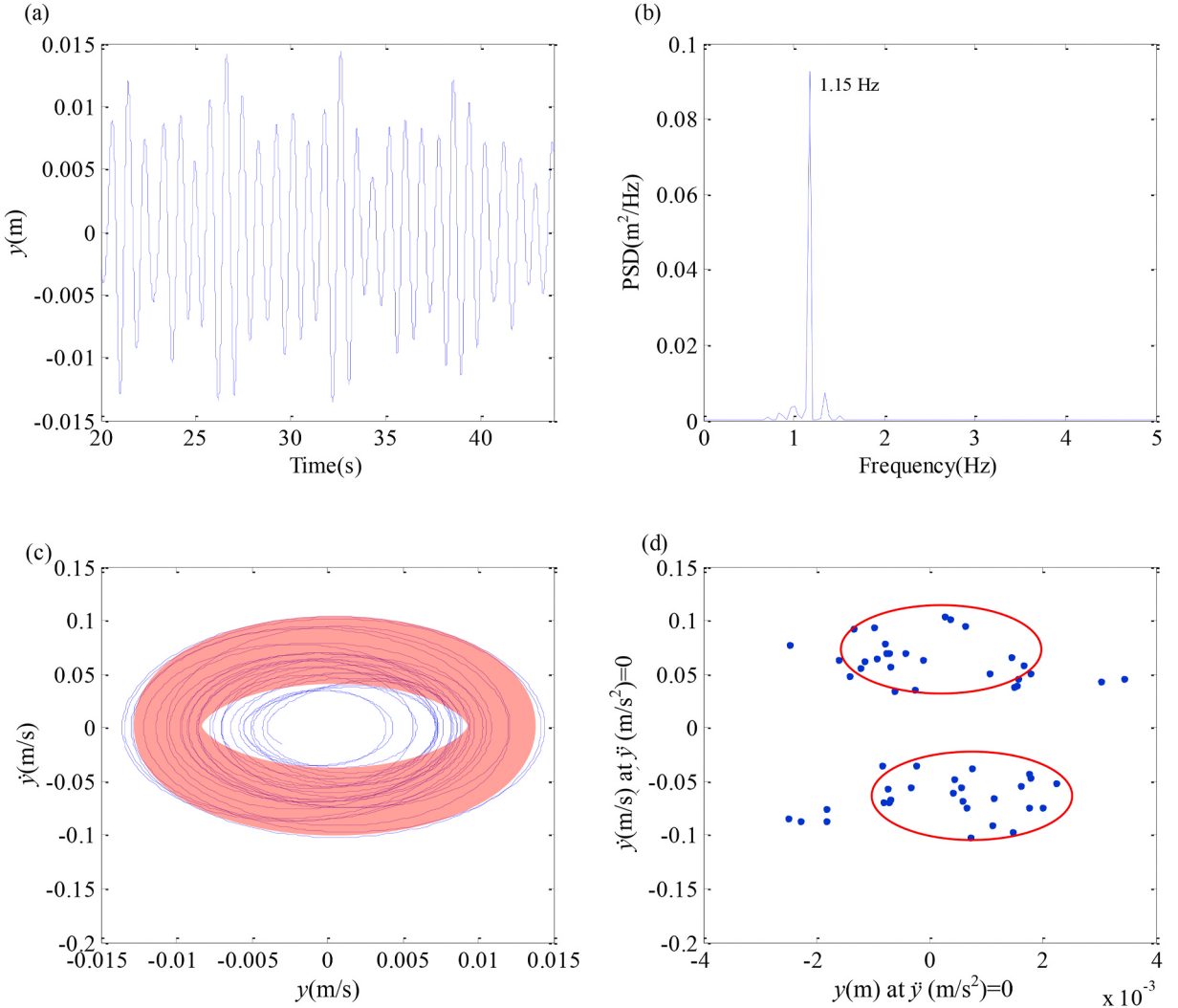


Fig. 25. (a) Time history, (b) PSD plot, (c) phase plane, and (d) Poincaré map of the entire signal at $x = 5.5$ m, case H A0105T596, with $A_{lm} = 0.105$ m, $T_{lm} = 5.96$ s; The time history is for the cross-flow displacement.

6. Conclusion

A method to identify vortex-induced forces and time-varying coefficients from measured strains of a Steel Catenary Riser (SCR) undergoing vessel motion-induced VIV is proposed. Euler-Bernoulli beam vibration equations with time-varying tension is adopted to describe the out-of-plane VIV responses. Vortex-induced Forces (VIF) are reconstructed via inverse analysis method, and the Forgetting Factor Least Squares method (FF-LS) is employed to identify time-varying vortex-induced force coefficients, including excitation coefficients and added mass coefficients. The method is verified via a finite element analysis procedure in commercial software Orcaflex which is well validated and widely used in SCR designs. The time-varying excitation coefficients and added mass coefficients of a SCR undergoing vessel motion-induced VIV are investigated. The following conclusions can be drawn:

- (1) In acceleration period of in-plane velocity, vessel motion-induced VIVs excite at the middle part of the SCR where excitation coefficients are positive and KC numbers are maximum; And then, the excited vibration waves travel to the ends of SCR in deceleration period, during which the excitation coefficient is around 0.
- (2) When parameter γ [1], which represents the significance of the local acceleration to the convective acceleration of in-coming flow, is larger than 0 (acceleration period of in-coming flow), most of the excitation coefficients are positive. The farther away γ is to 0, the larger the excitation coefficient value. When γ is negative (deceleration period of in-coming flow), the excitation coefficients are around zero or negative with range of -0.3 to 0.

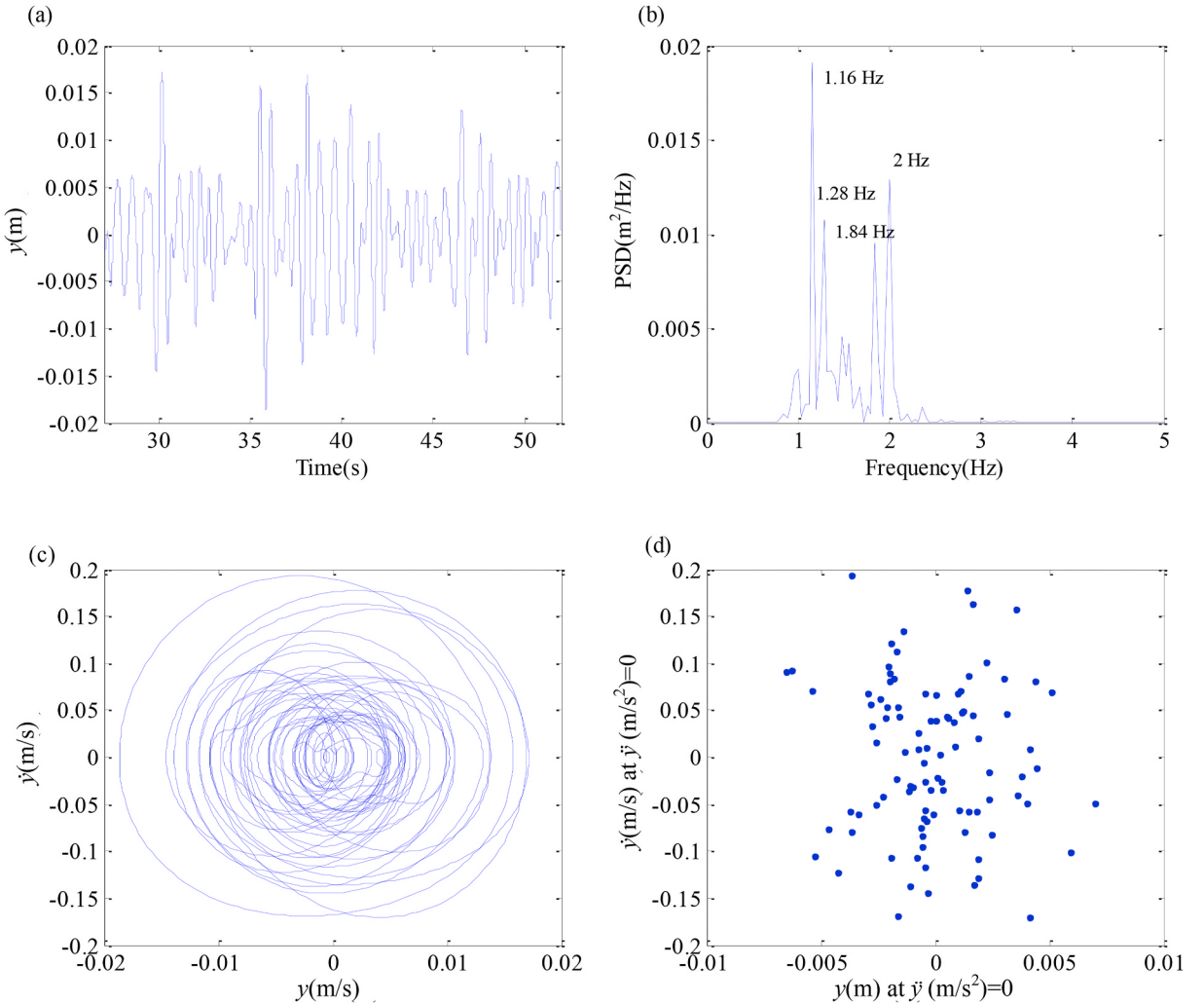


Fig. 26. (a) Time history, (b) PSD plot, (c) phase plane, and (d) Poincaré map of the entire signal at $x = 5.5$ m, case H A021T596, with $A_{in} = 0.21$ m, $T_{im} = 5.96$; The time history is for the cross-flow displacement.

- (3) Time-varying tensions have significantly positive correlation with added mass coefficients when T_r exceeds the range of 0.7–1.3. In addition, the added mass coefficients are basically around 1.0 when traveling wave occurs, while have significant variations when standing wave is dominant.
- (4) Chaotic characteristic is observed in both VIV responses and VIF coefficients, and it is more evident with the increase of vessel motion velocity.

In addition, it should be noted that the concluded results in this paper were checked and applicable for vessel motion induced VIV with relatively gentle vessel heave motions whose corresponding KC number is smaller than 90 and tension variation ratio T_r at the top end of SCR doesn't exceed the range of 0.4–1.6.

Results in this study have shown that the excitation coefficient and the added mass coefficient of vessel motion induced VIVs are affected by multiple parameters, such as γ , T_r , and V_r . It is suggested that these parameters should be used as the key parameters of load matrix design in the future tests for vortex-induced vibration of flexible risers under vessel motions or under oscillatory flow.

Declaration of competing interest

The authors declare that they have no known competing financial interests or personal relationships that could have appeared to influence the work reported in this paper.

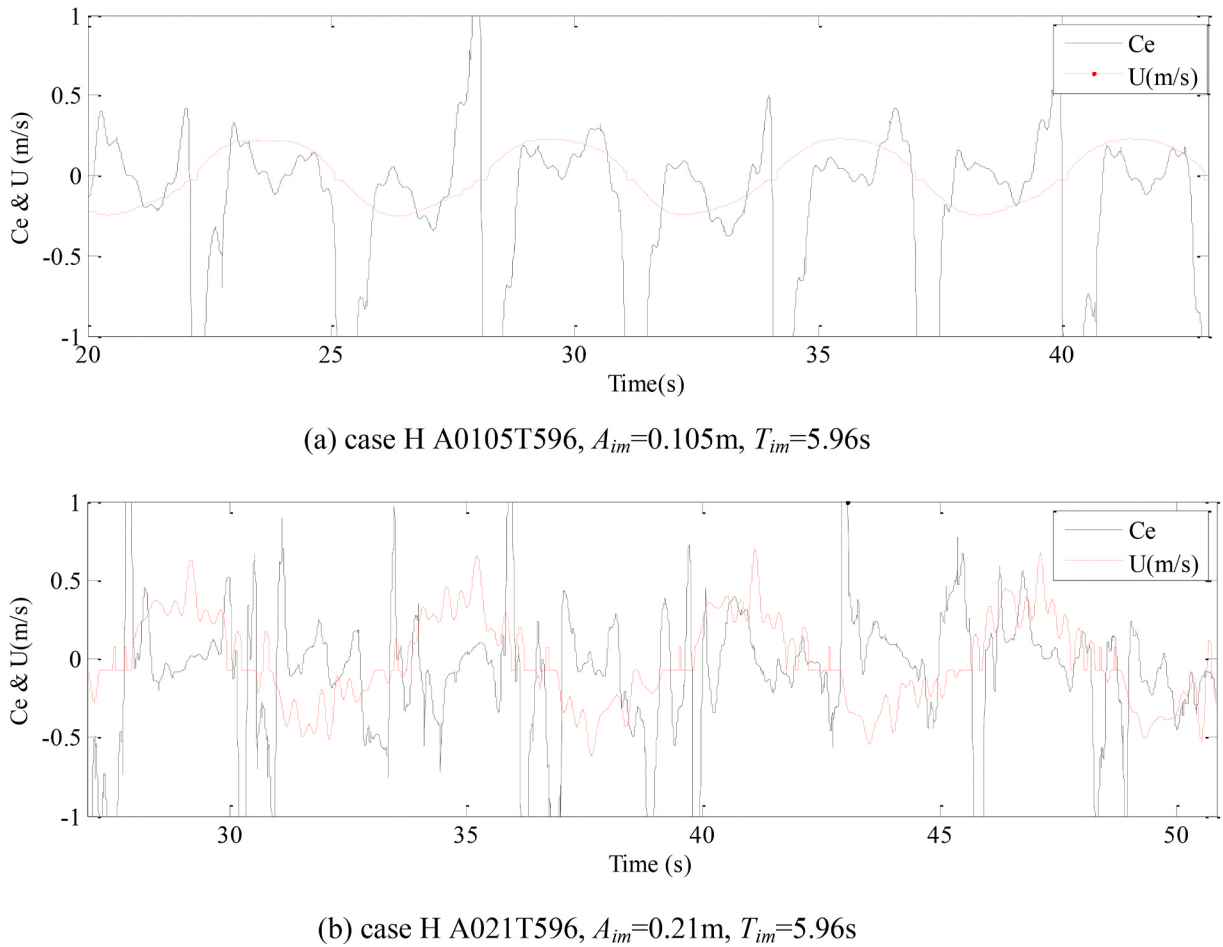


Fig. 27. Time histories of excitation coefficient and in-plane velocity at $x = 5.5$ m

Acknowledgements

The authors gratefully acknowledge the financial support from Equinor, Norway for the research program, Data analysis of heave-induced VIV measurements. Special thanks to Equinor for the permission of using their data for this publication. The support from the National Science Fund for Distinguished Young Scholars under Grant Number of 51825903, Program of Shanghai Academic Research Leader (Grant Number: 19XD1402000) the National Science and Technology Major Project of China (Grant Number: 2016ZX05028-001 and 2017YFC0804500) are also acknowledged.

References

- [1] Sarpkaya T. Nonimpulsively started steady flow about a circular cylinder. *AIAA J* 1991;29(8):1283–9.
- [2] Phifer EH, Kopp F, Swanson RC, Allen DW, Langner CG. Design and installation of Auger steel catenary risers. Houston, TX, USA: Offshore Technology Conference; 1994.
- [3] Morooka CK, Tsukada RI. Experiments with a steel catenary riser model in a towing tank. *Appl Ocean Res* 2013;43:244–55.
- [4] Wang J, Fu S, Larsen CM, Baarholm R, Wu J, Lie H. Dominant parameters for vortex-induced vibration of a steel catenary riser under vessel motion. *Ocean Eng* 2017;136:260–71.
- [5] Wang J, Xiang S, Fu S, Cao P, Yang J, He J. Experimental investigation on the dynamic responses of a free-hanging water intake riser under vessel motion. *Mar Struct* 2016;50:1–19.
- [6] Wang J, Fu S, Baarholm R, Wu J, Larsen CM. Fatigue damage induced by vortex-induced vibrations in oscillatory flow. *Mar Struct* 2015;40:73–91.
- [7] Wang J, Fu S, Baarholm R. Evaluation of vortex-induced vibration of a steel catenary riser in steady current and vessel motion-induced oscillatory current. *J Fluid Struct* 2018;82:412–31.
- [8] Fernandes AC, Mirzaeisefat S, Casc OLV. Fundamental behavior of vortex self induced vibration (VSIV). *Appl Ocean Res* 2014;47:183–91.
- [9] Lodahl CR, Sumer BM, Freds E J. Turbulent combined oscillatory flow and current in a pipe. *J Fluid Mech* 1998;373:313–48.
- [10] Fu S, Wang J, Baarholm R, Wu J, Larsen CM. Features of vortex-induced vibration in oscillatory flow. *J Offshore Mech Arctic Eng* 2014;136(1):1–10.
- [11] Ren H, Xu Y, Cheng J, Cao P, Zhang M, Fu S, Zhu Z. Vortex-induced vibration of flexible pipe fitted with helical strakes in oscillatory flow. *Ocean Eng* 2019; 189106274.
- [12] Liao JC. Vortex-induced vibration of slender structures in unsteady flow. Cambridge, MA, USA: Massachusetts Institute of Technology; 2002.

- [13] Thorsen MJ, S Vik S, Larsen CM. Fatigue damage from time domain simulation of combined in-line and cross-flow vortex-induced vibrations. *Mar Struct* 2015; 41:200–22.
- [14] Thorsen MJ, S Vik S, Larsen CM. Non-linear time domain analysis of cross-flow vortex-induced vibrations. *Mar Struct* 2017;51:134–51.
- [15] Gopalkrishnan R. Vortex-induced forces on oscillating bluff cylinders. Cambridge, MA, USA: Massachusetts Institute of Technology; 1993.
- [16] Aronsen KH. An experimental investigation of in-line and combined in-line and cross-flow vortex induced vibrations. Trondheim, Norway, NTNU; 2007.
- [17] Dahl J. Vortex-induced vibration of a circular cylinder with combined in-line and cross-flow motion. Cambridge, MA, USA: Massachusetts Institute of Technology; 2008.
- [18] Yin D, Lie H, Baarholm RJ. Prototype Reynolds number vortex-induced vibration tests on a full-scale rigid riser. *J Offshore Mech Arctic Eng* 2018;1(140):011702.
- [19] Song L, Fu S, Cao J, Ma L, Wu J. An investigation into the hydrodynamics of a flexible riser undergoing vortex-induced vibration. *J Fluid Struct* 2016;63:325–50.
- [20] Zhang M, Fu S, Song L, Wu J, Lie H, Ren H. Hydrodynamics of flexible pipe with staggered buoyancy elements undergoing vortex-induced vibrations. *J Offshore Mech Arctic Eng* 2018;140(6):061805.
- [21] Fu S, Lie H, Wu J, Baarholm R. Hydrodynamic coefficients of a flexible pipe with staggered buoyancy elements and stakes under VIV conditions. In: ASME 2017 international conference on ocean, Offshore and Arctic Engineering; 2017. V002T08A044.
- [22] Wu J, Lie H, Fu SX, Baarholm R, Constantines Y. VIV responses of riser with buoyancy elements: forced motion test and numerical prediction. In: ASME 2017 international conference on ocean, offshore and arctic engineering. Norway: Trondheim; 2017.
- [23] Liu C, Fu S, Zhang M, Ren H, Xu Y. Hydrodynamics of a flexible cylinder under modulated vortex-induced vibrations. *J Fluid Struct* 2020;94:102913 [Under review].
- [24] Wang J, Fu S, Baarholm R. Vortex-induced vibration of steel catenary riser under vessel motion. In: ASME 2014 33rd international conference on ocean, offshore and arctic engineering; 2014 [San Francisco, California, USA].
- [25] Orcina. OrcaFlex manual. 2017 [UK].
- [26] Sarpkaya T. Transverse oscillations of a circular cylinder in uniform flow, part 1. Monterey, CA, USA: Naval Postgraduate School; 1977.
- [27] Vandiver JK. SHEAR7 user Guide 4.5. Cambridge, MA, USA: Department of Ocean Engineering, Massachusetts Institute of Technology; 2003.
- [28] Larsen CM, Yttervik R, Passano E, Vikestad K. VIVANA theory manual. Norway: Trondheim; 2017. Version 4.10.1.
- [29] Swithenbank SB, Larsen CM. Occurrence of high amplitude VIV with time sharing. In: ASME 2012 31st international conference on ocean, offshore and arctic engineering; 2012 [Rio de Janeiro, Brazil].
- [30] Wang J, Fu S, Baarholm R, Zhang M, Liu C. Global motion reconstruction of a steel catenary riser under vessel motion. *Ships Offshore Struct* 2019;14(5):442–56.
- [31] Liu C, Fu S, Zhang M, Ren H. Time-varying hydrodynamics of a flexible riser under multi-frequency vortex-induced vibrations. *J Fluid Struct* 2018;80:217–44.
- [32] Ding F, Chen TW. Performance bounds of forgetting factor least-squares algorithms for time varying systems with finite measurement data. *IEEE Trans Circ Syst* 2005;52(3):555–66.
- [33] Paleologu C, Benesty J, Ciochina S. A robust variable forgetting factor recursive least-squares algorithm for system identification. *IEEE Signal Process Lett* 2008; 15:597–600.
- [34] Chavent G. Identification of distributed parameter systems: about the output least square method, its implementation, and identifiability. Darmstadt, Germany: 5th IFAC Symposium on Identification and System Parameter Estimation; 1979.
- [35] Cleveland WS, Devlin SJ. Locally weighted regression: an approach to regression analysis by local fitting, vol. 83. Publications of the American Statistical Association; 1988. p. 596–610. 403.
- [36] Levin & David. The approximation power of moving least-squares. *Math Comput* 1998;67(224):1517–32.
- [37] Allen JB. Short term spectral analysis, synthesis, and modification by discrete fourier transform. *IEEE Trans Acoust Speech Signal Process* 1977;3(25).
- [38] Zhang H, Rowley CW, D E A, C L N. Online dynamic mode decomposition for time-varying systems. *SIAM J Appl Dyn Syst* 2019;3(18):1586–609.
- [39] Fu B, Zou L, Wan D. Numerical study of vortex-induced vibrations of a flexible cylinder in an oscillatory flow. *J Fluid Struct* 2018;77:170–81.
- [40] Franzini GR, Pesce CP, Gon alves RT, Fujarra ALC, Mendes P. An experimental investigation on concomitant Vortex-Induced Vibration and axial top-motion excitation with a long flexible cylinder in vertical configuration. *Ocean Eng* 2018;156:596–612.
- [41] Depoit & Andre. Free rotation of a rigid body studied in the phase plane. *Am J Phys* 1967;35(5):424.
- [42] Month LA, Rand RH. An application of the Poincaré map to the stability of nonlinear normal modes. *J Appl Mech* 1980;47(3):645.
- [43] Modarres-Sadeghi Y, Chasparis F, Triantafyllou MS, Tognarelli M, Beynet P. Chaotic response is a generic feature of vortex-induced vibrations of flexible risers. *J Sound Vib* 2011;330(11):2565–79.
- [44] Chasparis F, Modarressadeghi Y, Hover FS, Triantafyllou MS, Tognarelli M, Beynet P. Lock-in, transient and chaotic response in riser VIV. In: ASME 2009 28th international conference on ocean, offshore and arctic engineering; 2009 [Honolulu, Hawaii, USA].